Bellot *et al.*
Cell Communication and Signaling (2024) 22:509
https://doi.org/10.1186/s12964-024-01883-5

Cell Communication and Signaling

RESEARCH

Open Access

Lanthanide conjugate Pr-MPO elicits anti-cancer activity by targeting lysosomal machinery and inducing zinc-dependent cataplerosis

Gregory Lucien Bellot[1†], Dan Liu[1,2†], Marc Fivaz[3,7], Sanjiv K. Yadav[1], Charanjit Kaur[4] and Shazib Pervaiz[1,2,5,6*]

Abstract

Acquired drug resistance is a major challenge in the management of cancer, which underscores the need for discovery and development of novel therapeutic strategies. We report here the mechanism of the anti-cancer activity of a small coordinate complex composed of the rare earth metal praseodymium (Pr) and mercaptopyridine oxide (MPO; pyrithione). Exposure of cancer cells to relatively low concentrations of the conjugate Pr-MPO (5 μM) significantly impairs cell survival in a p53-independent manner and irrespective of the drug resistant phenotype. Mechanistically, Pr-MPO-induced cell death is caspase-independent, not inhibitable by necrostatin, but associated with the appearance of autophagy markers. However, further analysis revealed incomplete autophagic flux, thus suggesting altered integrity of lysosomal machinery. Supporting the lysosomal targeting activity are data demonstrating increased lysosomal Ca^{2+} accumulation and alkalinization, which coincides with cytosolic acidification (drop in pH_c from 7.75 to 7.00). In parallel, an increase in lysosomal activity of glycosidase alpha acid (GAA), involved in passive glycogen breakdown, correlates with rapid depletion of glucose stores upon Pr-MPO treatment. This is associated with swift cataplerosis of TCA cycle intermediates, loss of NAD^+/NADH and increase in pyruvate dehydrogenase (PDH) activity to compensate for pyruvate loss. Addition of exogenous pyruvate rescued cell survival. Notably, lysosomal impairment and metabolic catastrophe triggered by Pr-MPO are suggestive of Zn^{2+}-mediated cytotoxicity, which is confirmed by the ability of Zn^{2+} chelator TPEN to block Pr-MPO-mediated anti-tumor activity. Together, these results highlight the ability of the small molecule lanthanide conjugate to target the cells' waste clearing machinery as well as mitochondrial metabolism for Zn^{2+}-mediated execution of cancer cells, which could have therapeutic potential against cancers with high metabolic activity.

Keywords Zinc, Cataplerosis, Lysosome, Intracellular pH, Pyruvate

†Gregory Lucien Bellot and Dan Liu contributed equally to this work.

*Correspondence:
Shazib Pervaiz
phssp@nus.edu.sg
Full list of author information is available at the end of the article

Introduction

Acquisition of therapy resistance is a major challenge in the management of cancer, which is facilitated by the high plasticity of cancer cells as well as tumor microenvironment and immunogenicity [1–6]. Therefore there is a need to re-deploy current anti-cancer strategies to reach a broader range of malignant targets, in particular targeting effector mechanisms underlying chemotherapy resistance.

One of the most commonly used class of chemotherapeutic agents are platinum-based molecules, such as cisplatin and carboplatin, which display anti-proliferative and pro-apoptotic activities by inducing DNA damage and oxidative stress [7, 8]. Despite their success in the clinical setting, this class of drugs is associated with adverse side effects and rendered ineffective due to the acquisition of drug resistance [9, 10]. Consequently, the therapeutic potential of other metal-based compounds is being evaluated [11]. To that end, lanthanides or rare earth elements have shown promise in applications ranging from diagnostics to potential therapeutics [12]. Lanthanides are a group of 15 metallic elements with an atomic number ranging from 57 to 71. They are chemically active electropositive metals displaying + 2 (europium and ytterbium) to + 4 oxidation state (cerium, terbium and praseodymium) and form stable compounds [13]. The chemical property of these rare earth elements to emit luminescence and/or fluorescence has been exploited for the design of probes and sensors for research and medical imaging [14–16]. For example, lanthanide-based molecules have found application as contrast agents, and recent evidence supports their potential use in radio-immunotherapy and photodynamic therapy [17–19]. In addition, advances in nanomaterials and nanomedicine have promoted the usefulness of lanthanides since lanthanide-doping appears to be an efficient method for enhancing the optical and biological properties of nanoparticles [20]. Notably, the ability of europium and lanthanum-based complexes to interact with lysophosphatidic acid (an ovarian cancer biomarker) and gangliosides has been proposed as a sensing method to track cancer biomarkers [21]. AGulX gadolinium-based nanoparticles promote radio-sensitization of tumors due to the capacity to accumulate within cancer cells, while displaying low toxicity [22]. Another gadolinium-based molecule, the metallofullerenol Gd@C82(OH)22 has shown promise as a neoadjuvant therapy to target tumor microenvironment and cancer stem cells [23]. Lanthanides have also been shown to compete with Ca^{2+} thus exhibiting higher affinity for Ca^{2+}-binding proteins and tissues [24]. Gadolinium has been shown to inhibit calcium channel [25], while cerium binds apo-transferrin and elicits cytotoxicity against Hela and MCF-7 cancer cells [26]. Lanthanum and cerium ions inhibit growth of gastric cancer cells by destabilizing microtubules [27] and elicit anti-proliferative effects against colorectal and hepatocellular carcinoma cell lines [28]. While the aforementioned reports provide limited insights into the biological effects of lanthanides, considering their potential for use in the clinical setting an in-depth understanding of cellular targets and molecular mechanisms is highly desirable.

Our group has been interested in studying the biological properties of the lanthanide, praseodymium (Pr), which together with cerium, gadolinium and neodymium is the closest to Ca^{2+} in terms of ionic radius length [13]. Pr has emerged as an ideal candidate for use in bioimaging and biosensing applications due to its wide range luminescence emitting property [29–31]. In this regard, the combination of $LuPO_4$:Pr^{3+} nanoparticles emitting UVC with X-ray were shown to sensitize hypoxic lung cancer to radiotherapy in vitro [32]. Moreover, Pr 142 has been investigated as a radionuclide in brachytherapy for hepatic tumors and uveal melanomas [33–35]. In this study, we investigated the anti-cancer activity of a coordinate complex of 2-mercaptopyridine N-oxide (MPO, also known as pyrithione) with Pr (Pr-MPO). Pr-MPO was designed to explore whether the lanthanide-conjugate significantly enhanced cytotoxicity of the original compound (MPO) while reducing the effective concentration required for the anti-cancer effect. To that end, our previous findings demonstrated cancer targeting activity of MPO [36, 37]. More recently, we linked the p53-dependent or -independent anti-cancer activity of MPO to inhibition of topoisomerase IIα activity [38]. Here we provide evidence that Pr-MPO elicits potent anti-cancer activity by promoting lysosomal Ca^{2+} accumulation and alkalinization, adversely affecting the TCA cycle, and triggering Zn^{2+}-dependent execution. Notably, Pr-MPO shows comparable effects in vitro and in vivo and targets cancer cells rendered resistant to conventional chemotherapy.

Materials and methods

Reagents and chemicals

Benzyloxycarbonyl-Val-Ala-Asp (OMe)-fluoromethylketone (Z-VAD-FMK), BAPTA-AM were purchased from ALEXIS, (NY, USA). Praesodymium oxide (Pr6O11), cobalt chloride ($CoCl_2$), ammonium persulfate (APS), necrotatin-1, 3-methyladenine (3-MA), wortmannin, pepstatin A, crystal violet, bromophenol blue, Tween 20, EGTA, HEPES, DTT, glycine, DMF, DMSO, Earle's Balanced Salt Solution (EBSS), bafilomycin A1, chloroquine, staurosporine, rapamycin, nigericin, were purchased from Sigma Aldrich Co (St Louis, MO). Acrylamide/bis-acrylamide (30% solution), Coomassie Plus Protein Assay Reagent and Protease Inhibitor Cocktail were obtained

from Pierce, (IL, USA). 10X PBS, 10X SDS, Tris-HCl buffer (pH7.4) were purchased from NUMI Media Preparation Facility (NUS, Singapore). Triton X-100 was obtained from USB, (OH, USA). Torin1 was purchased from Tocris Bioscience (Bristol, UK).

Synthesis and analysis of Pr-MPO

In a small flask Pr_6O_{11} (102.1 mg, 0.1 mmol) was dissolved in HCl (6 M, 10 mL). The solution was neutralized with a solution of NaOH (1 M) to pH = 5. A solution of MPO-Na (282.3 mg, 1.8 mmol, 95% active) in water was added. The solution was stirred for 2 h at 40ºC and then was cooled to room temperature to give green microcrystals, which were collected by filtration, washed successively with H_2O, EtOH, and dried *in vacuo*. Pale green prism crystals suitable for X-ray analysis were obtained by recrystallization of the precipitate from dimethyl sulfoxide. Analysis revealed: C, 33.81; H, 3.62; N, 6.28%. Calc. for $C_{19}H_{24}N_3O_5S_5$ Pr: C, 33.78; H, 3.58; N, 6.22%); IR ($cm^{-}1$): 1141(s, C S), 1090 (s, N O); UV-vis (DMSO): 290, 346 nm. *Crystal Data* : M. Formula = $C_{19}H_{24}N_3O_5S_5Pr$, M W = 675.62; Crystal system : Triclinic, Space group $P^{-}1$; Unit cell dimensions (4148 *a* = D 9:570(2)°A; reflections in full μ range) *b* = D 9:902(2)°A, *c* = D 15:743(3)°A, *Alpha* = D 89:00(3)±, *Beta* = D85:54(3)±, *Gamma* = D 62:97(3)± Final *R* indices [$I > 2gI$)] *R1 = D 0:0352, wR2 = D 0:0706.*

Cell lines and cell culture

The human cervical carcinoma Hela cell line was purchased from American Type Culture Collection (ATCC, MD, USA), and cultured in Dulbecco's Modified Eagle Medium (DMEM, GE Healthcare Life Science, Utah, USA) supplemented with 1% L-glutamine, 1% penicillin/streptomycin (Hyclone, Thermo Fisher Scientific, MA, USA) and 10% fetal bovine serum (FBS, Hyclone, CA, USA). Hela cell line stably expressing a FRET probe fused with a Caspase 3 recognition motif (DEVD-FRET) was a generous gift from Dr. Qian Luo (Nanyang Technological University, Singapore). Human breast cancer cell lines, MDA-MB-231 and MCF-7 were purchased from American Type Culture Collection (ATCC, Rockville, MD) and maintained in Roswell Park Memorial Institute 1640 medium (RPMI, Hyclone, Utah, USA) supplemented with 1% L-glutamine, 1% penicillin/streptomycin and 10% FBS. Mouse embryonic fibroblasts WT MEF and *Atg5 KO* MEF cell lines were generously granted by Dr. Noboru Mizushima (The University of Tokyo, Graduate School and Faculty of Medicine, Tokyo, Japan) and maintained in DMEM medium supplemented with 1% L-glutamine, 1% penicillin/streptomycin and 10% FBS. Human colorectal carcinoma HCT116 WT, HCT116 *p53 KO* and HCT116 *Bax/Bak DKO* cell lines were generously provided by Dr. Bert Vogelstein (The Johns Hopkins University School of Medicine, Baltimore, MD) and maintained in McCoy5A (Gibco® Invitrogen Corporation, Carlsbad, CA) supplemented with 1% L-glutamine and 1% penicillin/streptomycin and 10% FBS. All cell lines were maintained in a humidified incubator at 37 °C with 5% CO_2 and propagated according to suppliers' recommendations.

Xenograft animal model

Tumor inoculation was performed by injecting human prostate cancer cells DU145 subcutaneously into female BALB/c nude mice ($n = 5$)/group as per the approved guidelines of the Institutional Animal Care and Use Committee (IACUC). When tumors reached a mean volume of 50 mm^3, Pr-MPO (5, 10, 20 mg/kg) was administered intraperitoneally 3-times a week for a total duration of 21 days, whilst the control group of mice only received solvent (DMF) injections. Tumor volume and body weight of mice were measured and recorded throughout the duration of the study. At the end of the experiment, mice were euthanized and tumors were collected for comparison between groups.

Crystal violet staining and small interference RNA gene silencing

The cytotoxicity effects of Pr-MPO and various pharmacological reagents or stimuli were determined by staining the treated cells with crystal violet and measuring the viable cell count by correlating with the absorbance values. Hela cells (1×10^5/ well) were seeded in triplicates in a 24 well plate one day prior to drug treatment. At the end point of drug treatment, culture medium was carefully discarded and cells were washed once with 1x PBS, stained with 200 µl of 0.1% crystal violet solution (prepared in 10% methanol) per well and incubated on the shaker for 10 min at room temperature. Subsequently, crystal violet solution was disposed into a cytotoxic waste container and cell plate was gently washed with deionized water until the water no longer ran dark. The plate was drained by inverting a couple of times on a tissue paper, followed by the addition of 500 µl of 1% SDS solution (prepared in 1x PBS) into each well to solubilize the crystals. Absorbance was measured with a TECAN Spectrophotometer (Tecan Trading AG, Switzerland) at 570 nm. Percentage of cell viability was calculated relative to the untreated control cells (presented as 100%). At least three independent experiment were performed in triplicates to obtain statistical significance. For gene silencing, ON-TARGETplus SMARTpool *siRNA* (pool of 4 single *siRNAs*) targeting human *Atg5*, *Atg7*, *RIP1* or *RIP3* as well as a scrambled *siRNA* control were purchased from Dharmacon Technologies (ThermoFisher

Scientific, Lafayette, CO, USA). Gene specific *siRNA* was introduced into cells using DharmaFECT1 reagent (ThermoFisher Scientific, Lafayette, CO, USA) according to the manufacturer's instructions. Briefly, HeLa cells to be transfected were grown to 40% confluence in 6-well plates on the day of transfection. Each *siRNA* was diluted with 250µL of Opti-MEM (Gibco, ThermoScientific, MA, USA) to attain a final concentration of 50nM; in another tube 5µL DharmaFECT was mixed with 250µL of Opti-MEM. Both solutions were gently mixed and incubated for 5 min at RT. The two solutions were combined by gentle pipetting and the resultant complex with a total of 500µL was incubated for 20 min at RT. Finally, 500µL of *siRNA* complex was carefully added into the wells and gently mixed by rocking the plates back and forth.

Colony forming assay

At the end point of drug treatment, Hela cells were washed with 1X PBS, trypsinized and counted. 10,000 cells were re-plated onto a petri-dish containing completed DMEM medium and kept in the incubator to allow colony formation over a period of 14 days. The culture medium was changed periodically. Cells were stained with crystal violet solution to visualize colonies; colony number and size were determined using the image analysis software Image J (http://imagej.nih.gov/ij/) to assess colony forming capabilities of individual sample. Only populations containing more than 20 cells were considered as colony units.

Analysis of cell viability using propidium iodide

Necrotic cells are usually defined by lack of integrity of plasma membrane, which can be labelled with propidium iodide (PI) staining and measured by flow cytometry. 2.5×10^5 Hela cells were harvested by trypsinization after periodic exposure to drugs. After washing twice with cold 1X PBS, cells were stained with 1 µM PI solution (prepared in cold 1x PBS) and filtered before flow cytometry (CyAn ADP, Beckman Coulter, USA). 10,000 events were collected with the excitation set at 488 nm and emission at 610 nm. Data were collected and analysed with WinMDI software (Windows multiple document interface for flow cytometry, Beckman Coulter Inc., Sunnyvale, CA). Dot plots with a gate drawn around a population of dead cells were adopted to present the results.

Detection of Caspase 3 activity

Caspase 3 activity assay was performed with a Hela stable cell line constitutively expressing caspase3-specific FRET biosensor (ECFP-DEVD-EYFP) to track apoptosis induction. Cells were plated onto a 48-well plate and incubated with indicated doses of Pr-MPO for 18 h. After treatment, cells were washed with 1x PBS and subjected to TECAN spectrophotometer for fluorescence readout detection. The final relative fluorescence units (RFU) was normalized against protein concentration of samples. The plotted X-fold decrease in RFU was inversely proportional to the increase in caspase 3 activity.

SDS-PAGE and Western blot analysis

Whole cell lysate was extracted with 0.1% Triton X-100 cell lysis buffer containing protease and phosphatase inhibitors. Protein concentration was quantified and equal amount of protein (30-40 mg) was prepared with 5x Laemmli loading dye and boiled at 100 °C for 5 min. Denatured protein samples were then subjected to sodium dodecyl sulphate-polyacrylamide gel electrophoresis (SDS-PAGE) with 8, 10, 12 or 15% (v/v) of acrylamide resolving gel depending on the molecular weight. Kaleidoscope pre-stained standards (Bio-Rad, CA, USA) were used to indicate the molecular sizes of the resolved protein bands. Subsequently, proteins separated on the gel were transferred onto PVDF membrane (Bio-Rad, CA, USA) using the wet transfer method at 350 mA for 1 h in an ice bath. Transferred membrane was then blocked with blocking buffer for 1 h on the shaker. Membrane was washed 3-times with 1x TBST before probing for the target proteins with correspondent primary antibodies at 4 °C overnight. On the following day, membrane was washed 3-times (10 min each time) with 1X TBST to avoid non-specific binding with excess primary antibodies and probed with appropriate HRP-conjugated secondary antibody solutions for 1 h at room temperature. For signal visualization, after three washes, membrane was incubated with Chemiluminescent Plus Western Blot Enhancing Kit (Merk Millipore, Darmstadt, Germany) and developed with X-ray film (Medical X-ray Processor, Kodak, NY, USA). Primary antibodies specific for PARP, Caspase 3, Bax, LC3B, phospho-mTOR, mTOR, phospho-4EBP1, 4EBP1, phospho-S6K, S6K, Atg5 and Atg7 were purchased from Cell Signaling Technology (Danvers, MA); QSTM1/p62, Bcl-2, β-actin and GAPDH were purchased from Santa Cruz Biotechnology (Santa Cruz, CA, USA). HRP-conjugated polyclonal secondary antibodies for anti-rabbit and anti-mouse were purchased from Thermo Fischer Scientific (Wilmington, DE, USA).

Transmission electron microscopy

Hela cells were seeded in a 4-well glass bottom chamber and incubated with 5µM Pr-MPO at indicated time points, followed by fixation for 2 h in 0.1 M Sorensen's Phosphate buffer ($Na_2HPO_4 \cdot 2H_2O$ 35.61 g dissolved in 1 L dH_2O, pH 7.4) containing 2.5% glutaraldehyde (EM grade) at room temperature. The specimen was washed 3-times with PBS and incubated in Sorensen's Phosphate buffer overnight at 4 °C. Specimens were then embedded

in plastic, sectioned, and stained with uranyl acetate and lead citrate. Thin sections were imaged on a JEOL 1230 EX transmission electron microscope. Images were acquired by Gatan ES500W Erlangshen camera with 1350 × 1040 pixels.

Live cells immunofluorescence microscopic analysis

HeLa cells (25,000 cells per well) were seeded onto a 4-well glass bottom chamber (Lab-Tek® Chamber Slides, Thermo Scientific Nunc, Wilmington, DE, USA) and transfected with green fluorescent protein conjugated LC3B (LC3B-GFP). 24 h post-transfection, cells were treated with 5 μM Pr-MPO for 3 and 6 h followed by three washes with 1x PBS. Subsequently, cells were fixed with paraformaldehyde (4% w/v) for 30 min and permeabilized with 0.5% Triton X-100 solution for 5 min at room temperature. To remove the remaining fixative thoroughly, cells were washed with 1X PBS for 3-times at each interval of 10 min and subjected to FluoView FV10i confocal microscopy system (Olympus, Hamburg, Germany). The fluorescence of GFP was excited by 488 nm spectral line of the argon-ion laser. Fluorescent images were acquired and analysed with Image J software.

Live-cell confocal imaging for intracellular calcium measurement

Time-lapse confocal microscopy experiment was performed on an inverted Eclipse TE2000-E microscope (Nikon, Melville, NY) equipped with a spinning-disk confocal scan head (CSU-10; Yokogawa, Tokyo, Japan), an autofocusing system (PFS; Nikon), and a temperature/CO_2-controlled automated stage. Images were acquired with a Cool SNAP HQ2 charge-coupled device camera (Photometrics, Tucson, AZ) driven by MetaMorph 7.6 (Molecular Devices, Sunnyvale, CA). For short-term imaging (up to 10 min) cells were imaged in complete DMEM medium at 37 °C supplied with 5% CO_2.

Fluo4-AM is a cell permeable, green-fluorescent calcium indicator for detecting intracellular calcium. Fluo 4-AM stock solution was prepared with Pluronic F-127 20% (w/v) solution in DMSO to a concentration of 2 mM. BCECF-AM is a cell permeable, red-fluorescent pH sensor for detecting intracellular H^+. BCECF-AM stock solution was prepared in DMSO to a concentration of 2 mM. Calcium Green-1 dextran (Potassium Salt, 10,000 MW) is a cell impermeable, green-fluorescent calcium indicator. Stock solution was prepared by dissolving it with dH_2O to a final concentration of 10 mg/ml. Texas Red dextran (Potassium Salt, 7,000 MW) is a cell impermeable, calcium-insensitive, red fluorescence probe. Texas Red stock solution was prepared with dH_2O to a final concentration of 5 mg/ml. 10 mg/ml stock solution of Oregon Green dextran (10,000 MW), a hydrophilic green fluorescent probe for detecting H^+, was prepared with dH_2O. MetaMorph time series images (stacks) were analysed with Image J software. Fluorescence intensity within the chosen ROI (the entire cell or several areas within the cells) was analyzed over the whole series of fluorescent images.

Intracellular pH measurement

pH calibration is a crucial determinant ensuring an accurate and quantitative outcome in the detection of intracellular pH. The simplest way to calibrate pH is to employ a series of buffers of different pH values, with which a standard pH calibration curve is generated. To do so, pH calibration buffer comprising 25 mM Na_2HPO_4 and 25 mM KH_2PO_4 dissolved in distilled water was prepared. Calibration buffer of a series of pH values ranging from 6.4, 6.8, 7.2, 7.6, 8.0 were adjusted with HCl or NaOH. Hela cells (7,500 cells) were seeded onto 48-well plate 18–24 h before the measurement of intracellular pH. On the day of the experiment, cells in triplicates were incubated with 5 μM Pr-MPO for a short duration of 2, 5–10 min. Treated cells were then washed 3-times with 1X HBSS buffer and loaded with fluorescence pH indicator solution containing 2μM of BCECF-AM at room temperature for 30–45 min. Cells were washed with 1X HBSS buffer thoroughly to remove the remnant dye and the emission fluorescence representative of intracellular H^+ concentration was measured using excitation λ of 485 nm and emission λ of 535 nm. Cell samples designated for pH calibration were incubated in buffers of different pH values and followed the same dye loading procedure as mentioned above. Before measurement of emission fluorescence, 10 μM of nigericin was added to equilibrate intracellular pH with the extracellular buffer pH.

GAA activity assay

Treated cells were harvested, washed twice in ice cold PBS and pelleted at 1000 g for 5 min. Cell pellet was resuspended in 150–250 μL Sodium Acetate 0.1 M, pH 4.0 and homogenized by pipetting up and down before leaving on ice for 30 min with two to three quick vortex cycles during the incubation. The solution was then centrifuged for 10 min at 16,000 g, 4 °C to remove all debris. The collected supernatant was used to measure protein concentration in the sample using the BCA protein assay (Thermo Fisher Scientific, Waltham, MA, USA). The volume of sample tested (2 to 5 μg of proteins per reaction) was loaded in 96-wells plates and the volume was then adjusted to 48.5 μL before adding 1.5 μL of 4-methylumbelliferyl α-D-glucopyranoside 100 mM. The plate was incubated at 37 °C from 0 to 6 h. Before

each measurement, 117 µL of glycine 0.4 M, pH 10.8 was added to stop the reactions and induce fluorescence of 4-methylumbelliferone released by the enzymatic activity of GAA. Fluorescence was measured on a Tecan M200 plate reader (Ex λ of 365 nm; Em λ of 450 nm). A standard curve of known quantities of 4-methylumbelliferone was used to determine enzymatic activity in the samples.

Metabolomics

The pellet of treated cells was resuspended with 300 µL of ice-cold deionized water containing 0.6% formic acid. A 30 µL aliquot was collected for protein content measurement. A volume of 270 µL of acetonitrile was added to the mix and vortexed before storage at -80° C. Samples were shipped and the organic acid panel was measured by Duke-NUS Metabolomics Facility (Duke-NUS Graduate Medical School, Singapore) as per their established protocols.

Measurement of glucose content, NAD^+/NADH and lactate

Measurements of total glucose, free glucose and glycogen were performed using the Glycogen Colorimetric/Fluorometric Assay Kit (BioVision, Waltham, MA, USA). Measurement of NAD^+/NADH was performed using the NAD^+/NADH Quantification Colorimetric Kit (BioVision, Waltham, MA, USA). Measurement of lactate content was performed using the Lactate Colorimetric/Fluorometric Assay Kit (BioVision, Waltham, MA, USA). All measurements were done following the manufacturer's instructions.

Statistical analysis

Data are presented as mean ± SEM where n corresponds to at least three independent experiments unless stated otherwise. Statistical significance was determined using one-way ANOVA followed by a post hoc Dunnett multiple comparison test, and two-tailed unpaired student's t-test as indicated in the figure legends with $p < 0.05$ considered statistically significant.

Results

Pr-MPO targets cancer cells irrespective of their drug resistant phenotype

Pr-MPO is comprised of a core Pr atom surrounded by three MPO and two DMSO molecules (Fig. 1A). MDA-MB-231 breast cancer cells, Hela cervical cancer cells and SHEP-1 neuroblastoma cells were treated with Pr-MPO (2.5 µM and 5 µM) for 18 h and cell viability was determined by crystal violet staining. A significant reduction of cell survival was observed with an IC_{50} of 5 µM (Fig. 1A), which was the concentration used in all subsequent experiments unless otherwise stated. Corroborating these data, a significant change in cell morphology (Fig. 1B) and tumor colony formation was observed (Fig. 1C). Using isogenic clones of HCT116 colorectal carcinoma cells, results showed no significant difference in the sensitivity of *HCT166 WT* or *p53KO* or *Bax/Bak DKO* cells to Pr-MPO, while the *p53KO* and *Bax/Bak DKO* cells were resistant to the conventionally used drug 5-Fluoruracil (5-FU) (Fig. 1D and E). Notably, A549 non-small cell lung carcinoma cells and their cisplatin-resistant counterpart 3CG cells also exhibited comparable sensitivity to Pr-MPO (Fig. 1F). Next, a xenograft murine model of DU145 cells was employed to assess the in vivo efficacy of intra-peritoneal administration of Pr-MPO (Fig. 1G). Results showed a significant inhibition of tumor growth in BALB/c nude mice (4 out of 5 as one mouse in the untreated group did not grow tumor) administered thrice weekly injections of Pr-MPO (5, 10 and 20 mg/kg) for 21 days (Fig. 1G and H). Notably, all mice survived through the duration of the study and did not elicit neurological symptoms such as changes in mobility, behavior or orientation and no untoward toxicity to the skin was observed. Also, mice in each group were weighed after each injection and/or drug treatment and no significant change (decrease or increase) in body weight was observed. Moreover, no significant histological changes were observed in the major organs of mice following treatment with Pr-MPO (Data not shown). Collectively, these data establish the potent anti-tumor activity of Pr-MPO in vitro and in vivo, and more importantly in cancer cells rendered defective in apoptotic execution or resistant to platinum-based chemotherapy.

(See figure on next page.)

Fig. 1 Pr-MPO induces cell death in a wide range of cancer cell lines. **A** The top panel shows the structure of Pr-MPO (praseodymium (2-mercaptopyridine N-oxide) (dimethyl sulfoxide)). The lower panel shows the effect of a dose response of Pr-MPO on HeLa, MDA-MB-231 and SHEP-1 cells assessed by crystal violet staining. **B** Light microscope observation and **C** Colony forming assay of HeLa, MDA-MB-231 and SHEP-1 cells untreated or treated with Pr-MPO 5µM. Comparison of cell sensitivity assessed through crystal violet staining **D** of HCT116 p53 wild type or p53 KO to increasing concentrations of 5FU or Pr-MPO, **E** of HCT116 wild type and HCT1116 $Bax^{-/-}$ $Bak^{-/-}$ to increasing concentrations of 5FU, doxorubicin and Pr-MPO and **F** of A549 and 3CG to increasing concentrations of cisplatin and Pr-MPO. **G** Xenograft protocol used to assess the ability of DU145 cells to form tumors in nude mice (top panel) and pictures of tumors collected from control and Pr-MPO treated animals (lower panel). **H** Evolution of tumor volumes in control and Pr-MPO treated animals

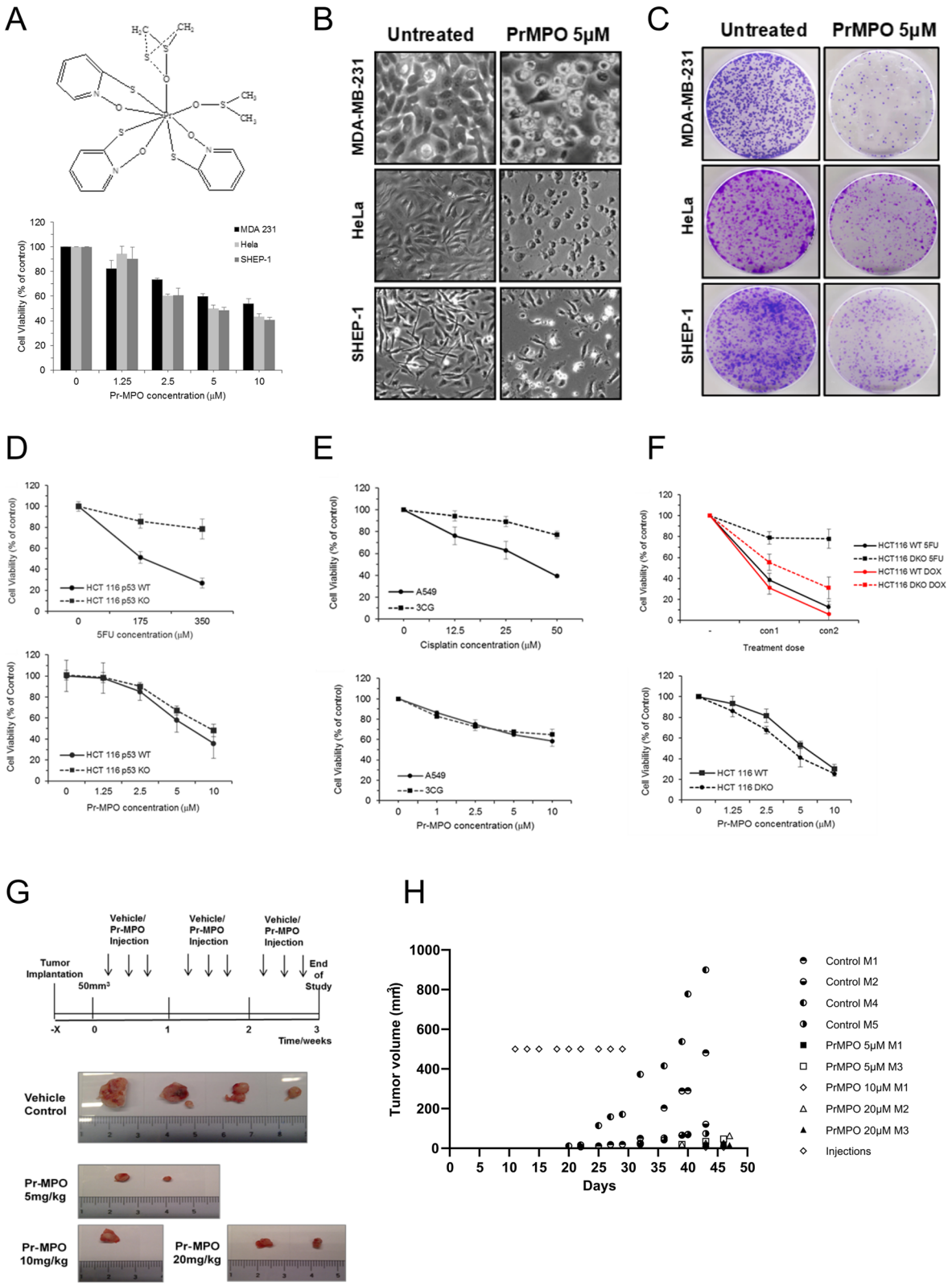

Fig. 1 (See legend on previous page.)

Pr-MPO-induced execution is caspase-independent and displays necrotic features

Next, we set out to investigate the mode of cell death triggered upon exposure to Pr-MPO. Firstly, flow cytometry and western blot analyses of apoptosis related proteins revealed no significant changes in cell cycle profile, caspase 3 activation, Bax or Bcl-2 expression, while a weak PARP cleavage at prolonged exposure (24 h) to the compound was detected (Fig. 2A and B). These data were corroborated by the inability of the pan-caspase inhibitor zVAD-fmk in rescuing Pr-MPO-induced cell death, unlike its effect on staurosporine exposure, thus ruling out the involvement of classical apoptosis (Fig. 2A). To further confirm these results, Hela cells stably expressing a caspase 3 FRET biosensor were employed as a reporter for caspase-3 activity. This construct consisted of a fluorescent donor (CFP) and an acceptor (YFP) with a linker sequence containing caspase 3 cleavage site. Caspase 3 activity is indicated by the decrease in emission fluorescence ratio between YFP (535 nm) and CFP (480 nm). The FRET model corroborated the inability of Pr-MPO to trigger caspase 3 activity, similarly to necrotic concentrations of hydrogen peroxide, but unlike staurosporine which strongly induced caspase-3 activation (Fig. 2C). Furthermore, morphological examination of Pr-MPO (5 µM for 18 h) treated HeLa cells using transmission electron microscopy revealed chromatin clumping, mitochondrial swelling, and increased vacuolization, which was suggestive of necrotic-like phenotype (Fig. 2D). However, a priori incubation with the necroptosis inhibitor, necrostatin-1, or gene silencing of *RIP1* (*siRIP1*) failed to rescue Pr-MPO mediated decrease in cell viability (Fig. 2E and F). Together, these data indicate that the anti-tumor activity of Pr-MPO does not involve classical apoptosis or necroptosis despite morphological features consistent with necrosis.

Autophagy is induced albeit stalled and does not mediate PrMPO-induced execution

Interestingly, Hela cells treated with 5 µM Pr-MPO for 3 h and 6 h showed an increase in canonical autophagy marker, LC3-II, together with a decrease in SQSTM1/sequestosome 1 (p62), an indicator of autophagy flux (Fig. 3A). Much like the classical inducers of autophagy i.e., amino acid deprivation and mTOR inhibition, while Pr-MPO exposure resulted in decreased Thr 389 phosphorylation of mTOR signaling targets S6K (Fig. 3A), the possibility of a decrease in the level of total S6K protein also cannot be ruled out. Transfection of Hela cells with GFP-LC3 vector also confirmed that Pr-MPO treatment promoted punctate LC3 staining, thereby indicating an autophagy-like phenotype (Figure S1). This was further investigated using transfection with a tandem fluorescence probe, mRFP-EGFP-LC3, to visualize autophagic flux, which is indicated by the quenching of EGFP fluorescence in lysosomal acidic environment while RFP fluorescence remains stable. Results show that Pr-MPO treatment resulted in the maintenance of yellow punctate staining indicating stable EGFP signal, thus suggesting incomplete autophagic flux (Fig. 3B). These data were confirmed using pharmacological inhibition of autophagy with bafilomycin A1 that prevents autophagosome/lysosome fusion. While bafilomycin A1 further increased LC3-II and p62 accumulation upon mTOR inhibition with Torin1, the combination with Pr-MPO treatment did not result in a similar increase thus suggesting stalled or incomplete autophagy (Fig. 3C, upper panel). Similar results were obtained with chloroquine, another inhibitor of lysosomal acidity (Fig. 3C, lower panel). Moreover, PI3 Kinase inhibitors 3-methyladenine (3MA) or wortmannin did not prevent cell death induced by Pr-MPO treatment; 3MA pre-treatment slightly reduced LC3-II conversion observed upon 5 µM Pr-MPO treatment (Fig. 3D, E and F). Last, while Pr-MPO failed to induce LC3-II in Hela cells transfected with *siRNA* against *Atg5* or *Atg7* as well as in *Atg5-KO* MEFs (Fig. 3G), gene silencing of *Atg5*

(See figure on next page.)

Fig. 2 Pr-MPO-induced cell death displays necrotic-like phenotypic features. **A** HeLa cells were pre-incubated with the pan-caspase inhibitor Z-VAD-FMK (25 or 50µM) for 2 h followed by 5µM Pr-MPO for 18 h. Apoptotic inducer staurosporine was used as a positive control at a concentration of 250nM. PI uptake was used to assess cell death using flow cytometry as described in Methods. **B** HeLa cells incubated with Pr-MPO for indicated durations were subjected to western blot analysis to test for pro-caspase 3 cleavage. **C** Caspase 3 activity was measured through fluorescence resonance energy transfer within a recombinant substrate stably expressed in HeLa cells containing cyan fluorescent protein (CFP) linked by a short peptide possessing the caspase 3 cleavage sequence, DEVD, to yellow fluorescent protein (YFP) i.e. CFP-DEVD-YFP). The bars represent means + SEM from three independent experiments. *, $p < 0.05$ and **, $p < 0.01$ compared with shRNA negative control cells receiving the same treatment. **D** Electron micrographs of HeLa cells treated with 5µM Pr-MPO. Arrows indicate mitochondrial swelling and chromatin clumping. **E** Necrostatin-1, a pharmacological inhibitor of RIP1, was administered to cells at indicated concentrations for 2 h, followed by 18 h treatment of 5µM Pr-MPO. Cell viability was subsequently conducted through crystal violet staining. **F** Gene silencing of *RIP1* was achieved by transfection of HeLa cells with 50nM *siRNAs* for 48 h. Post-transfected cells were subsequently incubated with Pr-MPO (2.5 and 5µM) for an additional 18 h. Effective silencing was assessed through western blot analysis while cell survival was evaluated through crystal violet staining

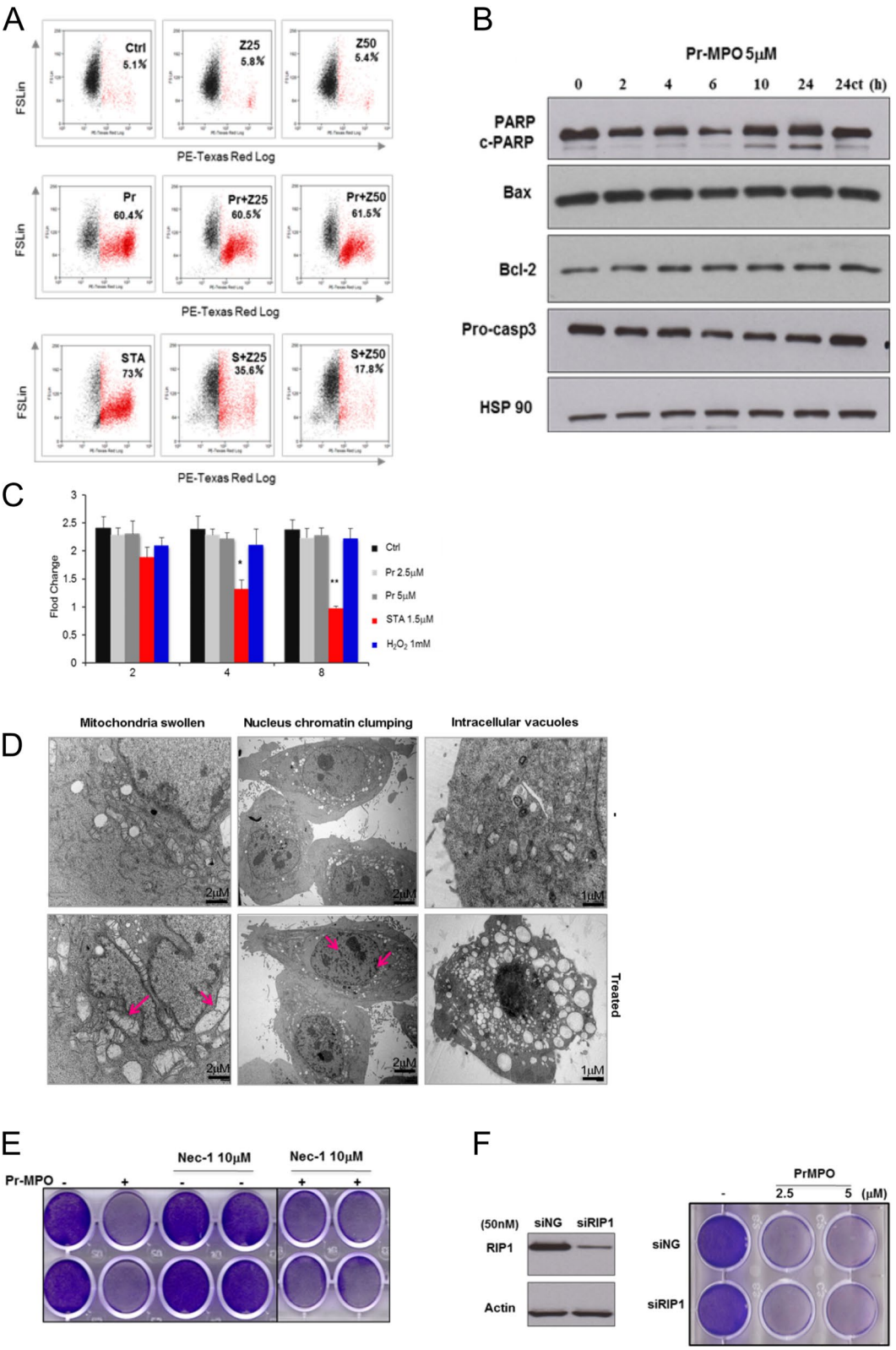

Fig. 2 (See legend on previous page.)

and *Atg7* did not inhibit Pr-MPO-induced cell death, as assessed by PI staining (Fig. 3H). These results demonstrate the ability of Pr-MPO to trigger autophagy, albeit incomplete, however, autophagy does not seem to be the mechanism underlying its anti-tumor activity.

Pr-MPO promotes lysosomal alkalization and intracellular Ca^{2+} accumulation

The mobilization of autophagic machinery even in the absence of complete flux suggested mTOR inhibition while implicating lysosomes in Pr-MPO induced cell death albeit independent of autophagy. Notably, lysosomal Ca^{2+} release has been shown to trigger mTORC1 activation [39], therefore, we questioned the possibility of Pr-MPO interfering with lysosomal Ca^{2+} mobilization. First, we observed that 100 µM $CoCl_2$ virtually completely blocked Pr-MPO induced cell death (Fig. S2A); Co^{2+} cations have been shown to block Ca^{2+} flux. Similarly, a priori treatment with 1 mM EGTA or 5 µM BAPTA-AM significantly alleviated Pr-MPO-dependent cell death with EGTA displaying stronger protection (Fig. 4A). These results were confirmed with PI staining showing a strong protective effect of these cation chelators (Fig. 4B, C and D). Also, $CoCl_2$ and EGTA, and BAPTA-AM to a lesser extent, inhibited Pr-MPO induced LC3-II conversion (Fig. 4E). Intrigued by these results, we next assessed intracellular Ca^{2+} using the Ca^{2+} sensitive fluorophore Fluo4-AM. Similarly to thapsigargin (2 µM), an inhibitor of sarco/endoplasmic reticulum Ca^{2+} ATPase (SERCA), Pr-MPO treatment initiated a quick fluorescence increase around 90 s in a dose dependent manner that continued to increase until plateauing (Fig. 4F and G and S2B). Moreover, high magnification analysis revealed peri-nuclear punctate fluorescence upon exposure to Pr-MPO (Fig. 5A, upper panel), which upon dual staining with lysotracker and Fluo4-AM confirmed the punctate appearance to be associated with the lysosomal compartment (Fig. 5A, lower panel). This punctate lysosomal fluorescence was absent in Hela cells pre-incubated with BAPTA-AM, $CoCl_2$ or when cultured in Ca^{2+}-free medium (Fig. 5B). One of the potential drawbacks of using Fluo4-AM is its ability to penetrate plasma membrane and susceptibility to intracellular esterase for activation; esterase activity can be found in many cellular compartments besides the cytosol therefore resulting in Fluo4-AM loading not only in the cytosol but organelles such as lysosomes. To address this possible bias, a dual two cell-impermeant dextran fluorescent probes was used, which consisted of the Ca^{2+} sensitive Calcium Green-1 dextran and the Ca^{2+} insensitive Texas Red dextran. Pre-loading was performed for 16 h to allow efficient lysosomal loading of the probes via endocytosis (Fig. 5C). Results showed that, upon exposure to Pr-MPO the Texas Red dextran signal remained stable while the Ca^{2+} Green-1 signal increased over time, thus indicating Ca^{2+} accumulation in the lysosomes (Fig. 5C), which could be inhibited by $CoCl_2$ and BAPTA-AM as well as upon removal of Ca^{2+} (Fig. 5D).

Next, we assessed the effect on intra-lysosomal pH using Hela cells pre-treated with the V-ATPase inhibitor Bafilomycin A1 (BfA1), which prevents lysosomal acidification. A priori incubation with BfA1 (1 µM for 2 min) completely inhibited the punctate Fluo4-AM signal upon Pr-MPO exposure without affecting the increase in overall fluorescence within the cytosol (Fig. 5E). These results were further verified using Ca^{2+} Green-1 and Texas Red dextran (Fig. 5F). Furthermore, to validate the importance of lysosomal pH variation in the biological activity of Pr-MPO, we made use of the pH-sensitive Oregon Green dextran and the pH-insensitive Texas Red dextran. Notably, similarly to the effect of BfA1, Hela cells treated with Pr-MPO displayed increased Oregon Green fluorescence within the lysosome, thus indicating lysosomal alkalinization (Fig. 5G). A reciprocal decrease in cytosolic pH was observed using the fluorescent pH indicator BCECF-AM; Pr-MPO (5–10 µM) decreased cytosolic pH

(See figure on next page.)

Fig. 3 Autophagy induced by Pr-MPO treatment is not responsible for Pr-MPO-mediated cell death. **A** HeLa cells were treated with Pr-MPO 5µM for indicated times as well as conventional autophagy inducers, 0.1µM Torin1, 0.5µM Rapamycin and amino acid (AA) depletion by incubating cells in EBSS buffer at indicated times. Cell lysates were collected and autophagy markers and mTOR substrates were analyzed through western blot. **B** HeLa cells at 24 h post-transfection with tfLC3 construct (EGFP-RFP-LC3) were treated with or without Pr-MPO 5µM for 3 h. Fluorescent images of LC3 punctuation/aggregation were acquired under each channel. **C** HeLa cells were pre-incubated with 10nM Bafilomycin A1 (top panel) or 20µM chloroquine (CQ) (lower panel) for 2 h before 3 h or 6 h treatment with Pr-MPO at 5µM. Torin1 (100nM, 3 h) served as a positive control of autophagic flux induction (top panel). Autophagic markers LC3II and p62 levels were tested through western blot analysis. **D** HeLa cells were pre-incubated with autophagy inhibitor 3-MA at 5mM for 2 h followed by 3–6 h 5µM Pr-MPO treatment before testing LC3 conversion through western blot. HeLa cells were pre-treated with either 5mM 3-MA or 50nM wortmannin (Wort) and cell death was assayed through **E** propidium iodide or **F** light microscopy and crystal violet staining. **G** HeLa cells were transfected with *siRNA* against *Atg5* and *Atg7* genes for 24 h before treatment with 5µM Pr-MPO for 3–6 h and tested for LC3 conversion through western blot (top panel). MEF wild-type (WT) or MEF Atg5 KO cells were treated with 5µM Pr-MPO for 3–6 h and tested for LC3 conversion through western blot (lower panel). **H** HeLa cells transiently transfected with 50nM of *siRNAs* targeting *Atg5* and *Atg7* or scrambled controls for 48 h were treated with 5µM Pr-MPO for 18 h. Cells were subsequently labelled with PI and cell death was measured using FACS analysis

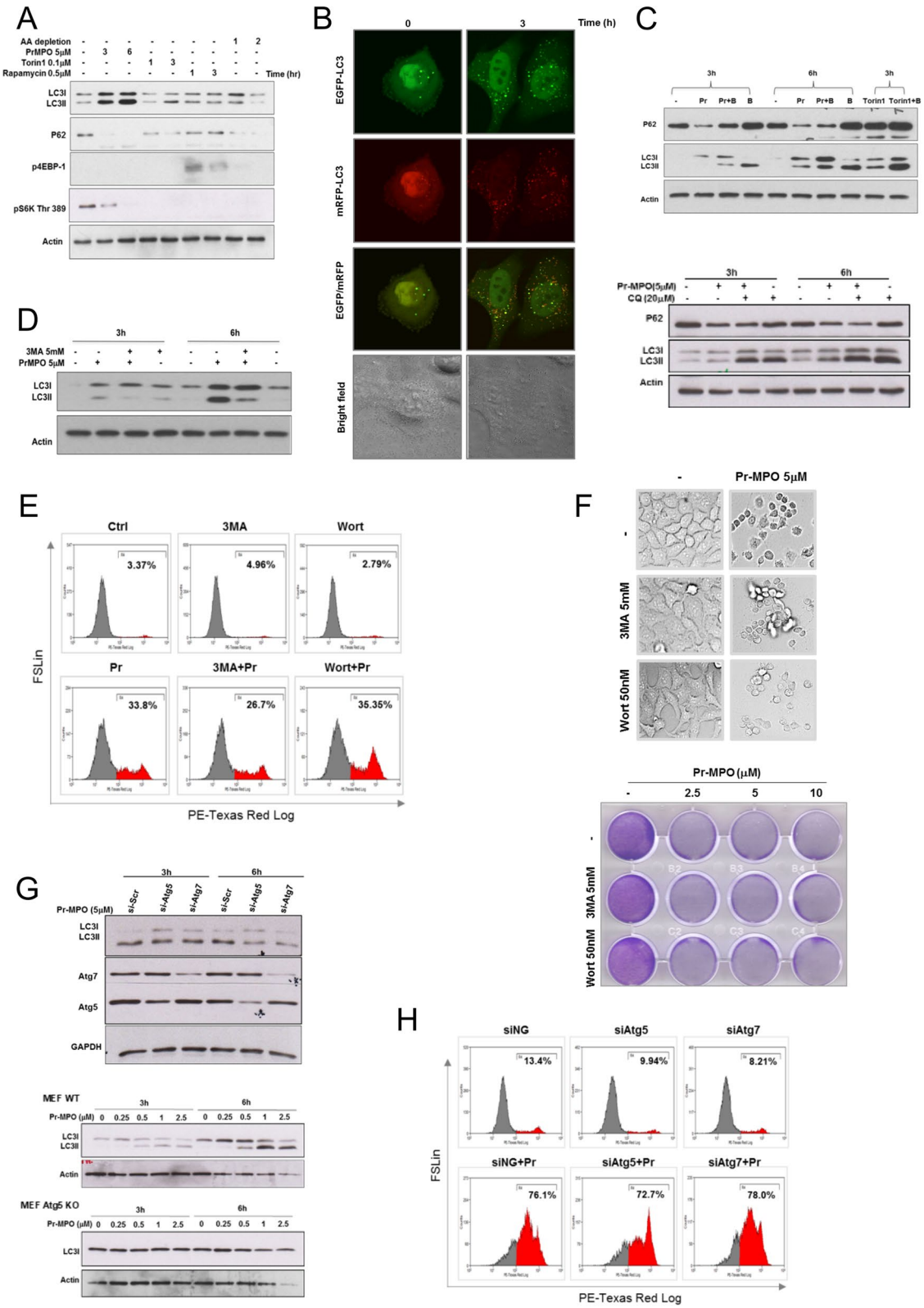

Fig. 3 (See legend on previous page.)

from 7.7 to 7.00 (Fig. 5H). Lysosomal homeostasis was also assessed by analysis of TFEB and its downstream target LAMP1. Phosphorylation of TFEB as well as increase in LAMP1 were detected in Pr-MPO treated cell lysates (Figure S3), suggesting lysosomal biogenesis. Notably, Ca^{2+} modulation failed to prevent TFEB activation and LAMP1 increase (Figure S3). Taken together, these results show that Pr-MPO promotes lysosomal Ca^{2+} accumulation and biogenesis together with an increase in intra-lysosomal pH and concomitant cytosolic acidification, however, suggest that lysosomal Ca^{2+} oscillations may not be the only mechanism of Pr-MPO induced execution.

Pr-MPO induces severe metabolic stress which is rescued by pyruvate

Intrigued by the lysosomotropic activity of Pr-MPO, we next assessed lysosomal metabolic pathways, in particular, activity of Glucosidase Alpha Acid (GAA), a lysosomal glycosidase involved in glycogen hydrolysis via a mechanism termed glycogen autophagy. GAA activity allowed the assessment of different parameters affected by Pr-MPO, i.e. autophagy induction, impact on lysosomal enzyme activity and overall cellular metabolism. Results showed a consistent increase in GAA activity in response to Pr-MPO (5 μM for 2 h; Fig. 6A), thereby suggesting increased glucose demand. The latter was verified by the significant decreases in total glucose and glycogen and concomitant increase in free glucose (Fig. 6B). Supporting these results, lactate and pyruvate levels rose within 30 min of exposure to Pr-MPO before steadily decreasing to a complete lactate depletion and significantly lower pyruvate levels (Fig. 6C). Furthermore, TCA intermediates, downstream of glycolysis and pyruvate, were also depleted upon Pr-MPO exposure (Fig. 6C). Indeed, while citrate remained relatively stable over time (Figure S4), succinate, malate, and fumarate, as well as α-ketoglutarate, appeared fully exhausted as early as one hour of Pr-MPO treatment (Fig. 6C). These results suggest increased glutamate dehydrogenase activity to sustain α-ketoglutarate for replenishing TCA cycle intermediates through anaplerosis. In addition, a strong decrease in NAD^+ levels as early as one hour of exposure to Pr-MPO provides testimony that the small molecule triggers a major metabolic crisis (Fig. 6D).

Stimulated by the data on Pr-MPO induced depletion of metabolites critical for the TCA cycle, we next asked if exogenous replenishment could rescue the phenotype. To test that, we supplemented medium with 5mM pyruvate before incubating HeLa cells with Pr-MPO (2.5-5μM for 4 h). Notably, a priori treatment with pyruvate almost completely rescued the effect of Pr-MPO (2.5μM) on tumor colony forming ability as well as enhanced overall survival (Fig. 6E). The central role of pyruvate depletion in the biological activity of Pr-MPO was further confirmed by its effect on pyruvate dehydrogenase (PDH) activity; phosphorylation at S293 residue indicates inhibition of PDH activity. Indeed, a significant decrease in PDH S293 phosphorylation was observed upon exposure to 5μM Pr-MPO, which started as early as 30 min and kept decreasing up to four hours following treatment (Fig. 6F). These results show that Pr-MPO treatment triggered an increase in PDH activity to compensate for the metabolic crisis, such as increased glucose demand and depletion of TCA metabolites. Furthermore, addition of exogenous pyruvate resulted in only a moderate decrease in PDH S293 phosphorylation, thus confirming the central role of pyruvate loss in the anti-tumor activity of Pr-MPO. Taken together, these data indicate that, even though cells compensate for the loss of pyruvate and TCA intermediates by increasing glucose mobilization and PDH activity, cell death is inevitable unless provided ectopic pyruvate to sustain cellular metabolism and survival.

Pr-MPO induces cell death through zinc-mediated toxicity

Interestingly, the rescue of Pr-MPO-induced cell death by exogenous pyruvate suggested a mechanism possibly involving zinc toxicity, known to be alleviated by pyruvate. Of note, MPO has also been shown to act as a zinc

(See figure on next page.)

Fig. 4 Pr-MPO appears to promote intracellular Ca^{2+} accumulation and Pr-MPO-induced cell death is inhibited by Ca^{2+} modulators. **A** HeLa cells were incubated with 1mM EGTA or 5μM Bapta-AM prior to 18 h treatment with 5μM Pr-MPO. Cell morphology was observed using transmitted light microscopy and cells survival was estimated through colony forming assay. HeLa cells were pre-treated **B** and **C** with or without 100μM $CoCl_2$ or **B** and **D** Ca^{2+} chelators EGTA (1mM) (**E**) and Bapta-AM (5μM) (**B**) Pr-MPO before subsequent treatment with 5μM Pr-MPO for 18 h. Cells attached on the plate and floating in the supernatant were collected and stained with propidium iodide for cell death assessment by flow cytometry. **E** HeLa cells were pre-treated with 100μM $CoCl_2$, 1mM EGTA or 5μM Bapta-AM followed by 2.5 or 5μM Pr-MPO treatment for 18 h before performing a western blot analysis of the autophagic markers p62 and LC3. **F** Time-lapse confocal imaging of HeLa cells loaded with 2μM intracellular Ca^{2+} indicator Fluo4-AM and treated with 2μM thapsigargin (top panel) or 5μM Pr-MPO (lower panel); each representative of at least three independent experiments. Scale bar, 20μM. **G** Relative fluorescence intensity (ΔF) values were determined over the initial fluorescence intensity of Fluo4-AM. Changes in Fluo4-AM fluorescence evoked by 2μM thapsigargin (left) or 5μM Pr-MPO (right) are shown as means ± SEM from 20 regions of interest (ROI) from a single coverslip, representative of at least three independent experiments

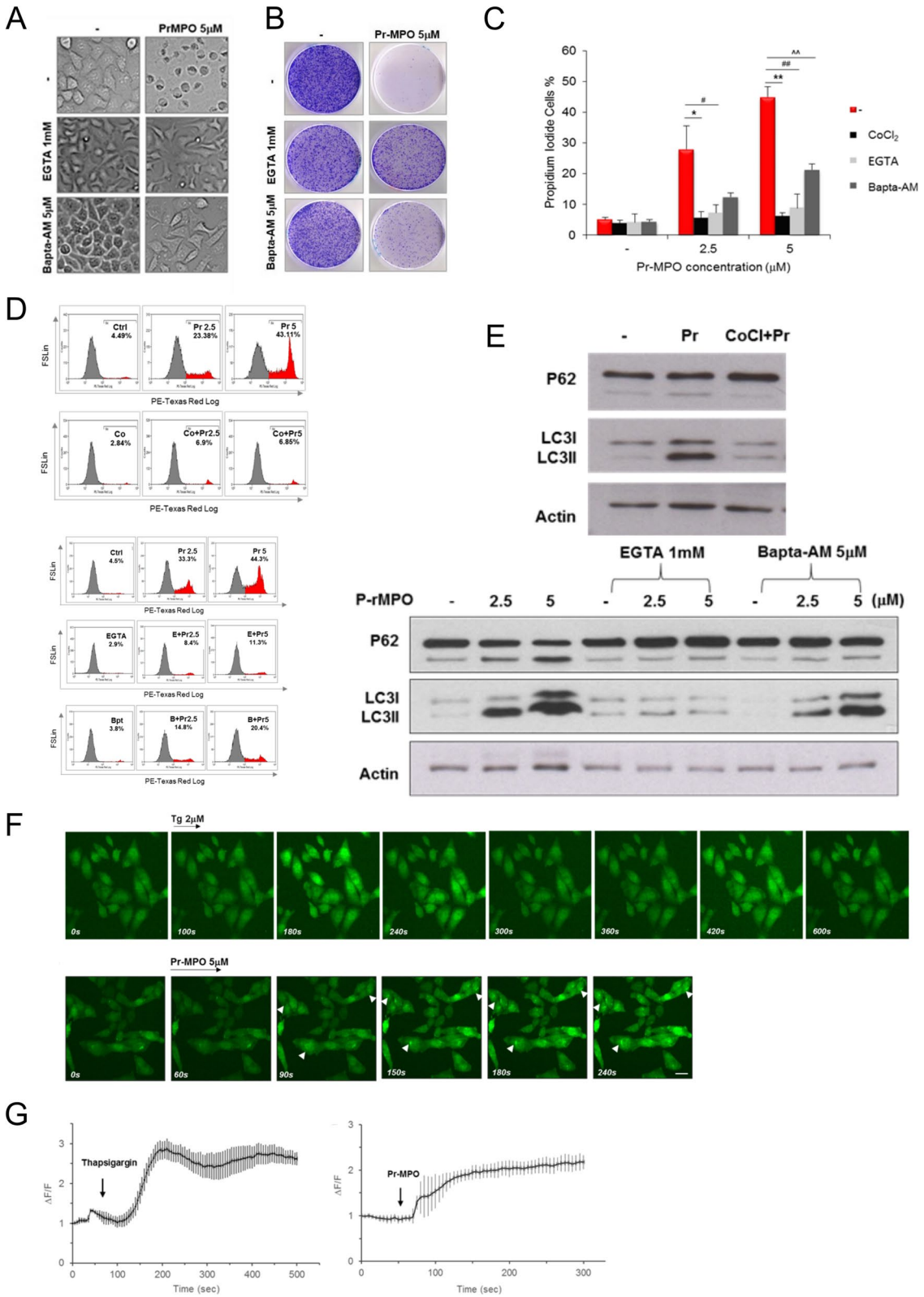

Fig. 4 (See legend on previous page.)

ionophore and therefore Pr-MPO appeared to retain this ability. First, to test the possibility that Pr-MPO promoted Zn^{2+} influx, we asked if FBS in the culture medium was the source of Zn^{2+}. Serum was deproteinized using trichloroacetic acid (TCA) protein precipitation method and either the deproteinized serum or the protein fraction was added to the culture medium. Results indicate that the effect of Pr-MPO was dependent upon the presence of FBS, as lowering the serum concentration ablated the effect on cell survival, which was restored upon progressively increasing FBS concentration, whereas the protein fraction of FBS had no effect on the biological activity of Pr-MPO (Figure S5A). Notably, the activity of Pr-MPO was restored in the presence of deproteinized serum (Figure S5A), thus suggesting that cell death induced by Pr-MPO was dependent on an element found in the non-protein fraction of serum. To test if Zn^{2+} was the factor responsible for the anti-tumor activity of Pr-MPO, serum-free medium was supplemented with 1 or 2μM sodium acetate or zinc acetate; culture medium supplemented with 10% FBS contains approximately 2.5μM of Zn^{2+}. Results show that the loss of activity in the absence of FBS was completely restored upon the addition of Zn^{2+} acetate to the culture medium (Fig. 7A). The latter was corroborated using a Zn^{2+}-specific chelator, TPEN, which blocked Pr-MPO-induced cell death (Fig. 7B). A similar effect was observed on tumor colony forming ability of HeLa cells with TPEN able to reverse the effect of Pr-MPO (Fig. 7C), thus strongly implicating Zn^{2+} in cellular toxicity. Furthermore, the inhibitory effect of Pr-MPO on PDH S293 phosphorylation could be mimicked by Zn^{2+} alone albeit at much higher concentrations and could be rescued by TPEN (Fig. 7D). Inhibiting autophagy with bafilomycin A1 did not affect Pr-MPO-induced decrease in PDH S293 phosphorylation (Fig. 7D), thereby suggesting that autophagy triggered by Pr-MPO was a stress response downstream of the metabolic changes. Interestingly, iron chelation with ethyl 3,4-dihydroxybenzoate (EDHB) also prevented PDH dephosphorylation (Fig. 7D), however, we believe that this effect might be attributed to the ability to promote HIF1α stabilization and upregulation of PDH kinase 1. Dichloroacetic acid, a PDH kinase inhibitor, was used as a positive control for blocking PDH S293 phosphorylation while LY303511 was used as a negative control (Fig. 7D). The fact that further addition of exogenous Zn^{2+} acetate (5μM) overcame the effect of TPEN argues in favor of an important role that Zn^{2+} stoichiometry plays in the anti-tumor activity of Pr-MPO (Fig. 7C and D).

Interestingly, Pr-MPO also induced an increase in lysosome biogenesis as evidenced by induced expression of TFEB and LAMP1 together with LC3 lipidation (Figure S5B). Lysosomal biogenesis is also corroborated by increased nuclear translocation of TFEB, a function of its dephosphorylation, upon exposure to Pr-MPO, which is rescued by TPEN but not pyruvate or EGTA (Figure S5C and D). These data provide evidence that the involvement of Zn^{2+} is upstream of the lysosomal effects induced by Pr-MPO, while exogenous pyruvate rescues the effect of Zn^{2+} on pyruvate depletion.

(See figure on next page.)

Fig. 5 Pr-MPO induces lysosomal Ca^{2+} accumulation and alkalinization as well as intracellular acidification. **A** Time lapse imaging (recorded over 5 min at 5 s interval) showing Fluo4-AM response of the same field of view of HeLa cells before and after application of Pr-MPO (top panel). HeLa cells were dual stained with Ca^{2+} indicator Fluo4-AM and LysoTracker® Red DND-99 (lower panel). **B** Time lapse images captured at 5-sec intervals over a total acquisition course of 5 min of the effect of 5μM PrMPO treatment alone or in presence of 5μM Bapta-AM, Ca^{2+}-free medium or 1mM EGTA in HeLa cells (top panel) and relative fluorescence intensity ΔF/F recorded as means ± SEM from at least three independent experiments in which 20 cells were quantified per experimental point (lower panel). **C** HeLa cells were cultured in DMEM medium containing 10 μg/mL Ca^{2+} binding indicator, Ca^{2+} Green-1 dextran (CG-1) and 5 μg/ml Ca^{2+} insensitive indicator, Texas Red dextran (TR) overnight. Loaded cells were washed and replenished with fresh medium for another 4 h followed by time lapse imaging analysis upon 5μM Pr-MPO treatment (left panel). effect of Pr-MPO on the emission intensity ratio of dual single-wavelength CG-1 and TR upon excitation of 488 nm and 564 nm. Data are representative of three independent imaging experiments. Statistical significance was calculated using $n = 30$ cells for each experimental point (right panel). **D** HeLa cells co-loaded with Ca^{2+} Green-1 and Texas Red and further pre-treated 2 h with 5μM Bapta-AM, 100μM $CoCl_2$ or 1mM EGTA-containing DMEM medium before 5μM Pr-MPO treatment. Time lapse confocal imaging was carried out at 5-sec intervals over a total acquisition duration of 5 min. **E** HeLa cells loaded with 5μM Fluo4-AM subjected to time-lapse confocal imaging. Intracellular Ca^{2+} level in response to Pr-MPO treatment was measured with or without proton pump inhibitor 1μM Bafilomycin A1 (left panel). The relative fluorescence intensity ΔF/F was recorded as mean ± SEM from at least three independent experiments (right panel). **F** Time-lapse imaging analysis of HeLa cells loaded with ratiometric Ca^{2+} probes CG-1 and TR for monitoring lysosomal Ca^{2+} changes upon 5μM Pr-MPO treatment alone or in presence of 1μM Bafilomycin A1 (top panel) and fluorescence curve of CG-1/TR emission fluorescence ratio over time. Statistical significance was derived from three independent experiments (lower panel). **G** Wide-field fluorescent imaging of HeLa cells loaded with dextran-conjugates Oregon Green (OG) and Texas Red (TR) in response to 5μM Pr-MPO or 1μM Bafilomycin A1 (top panel) and relative fluorescence of OG and TR probes measured within 7 min of Pr-MPO treatment and acquired 5-sec intervals over a total acquisition time course of 80 sec. **H** Measure of intracellular pH of HeLa cells untreated or treated with 5 or 10μM Pr-MPO for 2 h using cells loaded with 2μM BCECF-AM probe to determine the changes in pHi. Statistical analysis was performed using One-way ANOVA followed by a post-hoc Dunnett's multiple comparison test (**** $P < 0.0001$)

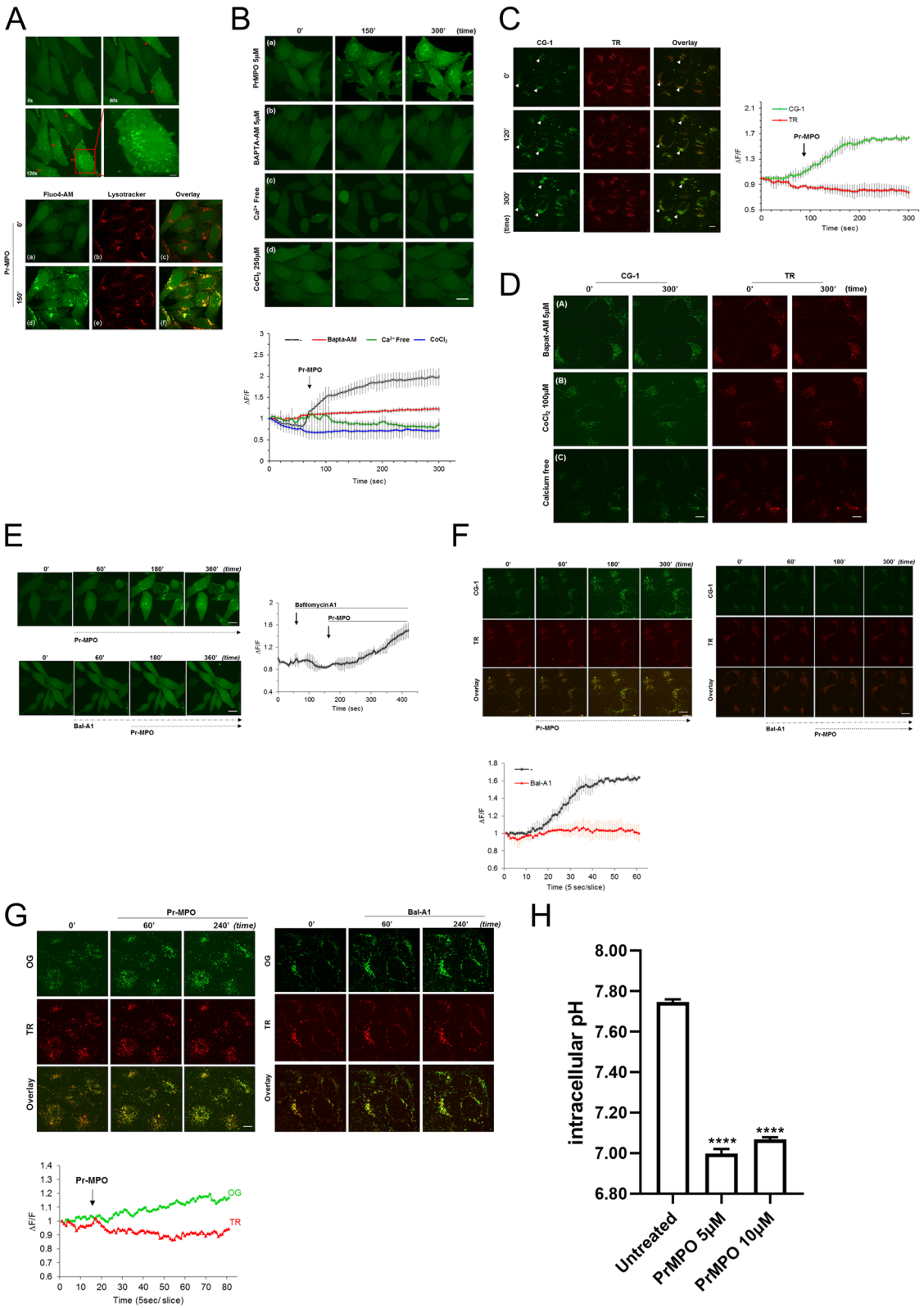

Fig. 5 (See legend on previous page.)

Next, to confirm the critical involvement of Zn^{2+} in the biological activity of Pr-MPO, we asked if Zn^{2+} modulation affected the decrease in glucose stores triggered by Pr-MPO. First, the effect of Zn^{2+} on total glucose, glycogen, lactate, and free glucose mirror imaged those obtained upon exposure to Pr-MPO; significant decreases in glucose, lactate, and glycogen with a concomitant increase in free glucose (Fig. 7E). Notably, while these changes triggered by Pr-MPO were rescued by TPEN, further increasing exogenous Zn^{2+} (10μM) could overcome the inhibitory effect of TPEN (Fig. 7E), thus supporting the critical role of Zn^{2+} in the metabolic changes induced by Pr-MPO. Similarly, Zn^{2+} chelation (TPEN) prevented the effect of Pr-MPO on cytosolic acidification, which could be overcome by the addition of excess Zn^{2+} (Fig. 7F).

To further validate Zn^{2+} influx as a critical mediator of the effect of Pr-MPO, the effect of Pr-MPO or its water-soluble analogue, Pr-MPO-NAC, on cell viability was assessed in the presence of 10μM or 50μM Zn^{2+}. As a reference, the core group MPO was used, which has previously been shown to promote Zn^{2+} uptake. Results show that the presence of Zn^{2+} significantly reduced the effective cytotoxic concentration of Pr-MPO, while a significantly higher concentrations were required for Pr-MPO-NAC or MPO (Figure S5E). These results indicate that higher availability of Zn^{2+} significantly reduced the concentration of Pr-MPO to achieve virtually complete inhibition of tumor cell survival, while the water-soluble analogue reduced the potency of the molecule. Also, conjugating the lanthanide Pr with three MPO groups (Pr-MPO) resulted in a significantly better anti-tumor activity compared to MPO (Figure S5E).

Discussion

Here we report that a novel lanthanide conjugate Pr-MPO triggered acute metabolic stress resulting in rapid depletion of intermediates associated with glucose catabolism, more specifically TCA cycle, and Zn^{2+}-mediated cytotoxicity. The anti-tumor activity of the small molecule conjugate was observed across a host of cancer cell lines, including those rendered refractory to apoptosis and/or conventional chemotherapy, and in a xenograft model. Although, phenotypic and biochemical analyses provided evidence for the presence of autophagy as well as ultrastructural features consistent with necrosis, results did not corroborate the involvement of apoptosis, autophagy or necrosis as the underlying execution mechanism; zVAD-fmk, necrostatin, *siRIP1* or pharmacological and genetic inhibition of autophagy did not block the effect of Pr-MPO on cell survival.

While autophagy was not critically involved in Pr-MPO induced anti-tumor activity, significant alterations in lysosomal machinery were observed, which could also explain the incomplete autophagic flux. Lysosome stress was also corroborated by the induction of lysosomogenesis as observed by nuclear localization of TFEB and increase in LAMP1 expression. Interestingly, a steady increase in lysosomal Ca^{2+} was observed upon exposure of cells to Pr-MPO, which was associated with lysosomal alkalinization. In addition, Ca^{2+} chelation not only blocked autophagy but also completely rescued cell viability. An earlier report showed that the release of lysosomal Ca^{2+} was an important factor in mTORC1 activation [39], and the fact that Pr-MPO promoted lysosomal accumulation of Ca^{2+} it is plausible that Pr-MPO triggers autophagy by preventing mTORC1 activation. However, the rise in intra-lysosomal pH in turn could prevent phagosome/lysosome fusion, necessary for complete autophagic flux [40], and hence the observed incomplete fluxing observed upon exposure to Pr-MPO. Notably, lysosomal alkalinisation was accompanied with intracellular acidification, thus creating an environment conducive for execution. In this regard, cancer cells have been shown to engage a reverse pH gradient to maintain an alkaline intracellular milieu which supports cell proliferation [41]. In addition, lysosomal function is a critical component of cancer cell growth via catabolism of cargos delivered through autophagy and macropinocytosis and mTORC1 activation which regulates anabolic functions [42]. Lysosomes also play an important role in the acquisition of drug resistance [43]. As such, intracellular acidification and impairment of lysosomal machinery are two important factors in the anti-tumor activity of Pr-MPO.

(See figure on next page.)

Fig. 6 Pr-MPO induces cataplerosis. **A** GAA activity measured in HeLa cells untreated or treated with 5μM Pr-MPO for 2 h. Unpaired two-tailed t-test was used for statistical analysis of the results of at least three independent experiments (*$P < 0.05$). **B** Measure of total glucose, free glucose and glycogen in HeLa cells untreated or treated with 5μM Pr-MPO for 2 h. Unpaired two-tailed t-test was used for statistical analysis of the results of at least three independent experiments (*$P < 0.05$, **$P < 0.01$). **C** GC-MS analysis of organic acids content measured in HeLa cells treated with 5μM Pr-MPO for 0, 30, 60, 120 and 240 min. Results show the combination of two independent experiments. **D** Measurement of NAD^+ and NADH content in HeLa cells untreated or treated with 5μM Pr-MPO for 2 h. Statistical analysis was performed using One-way ANOVA followed by a post-hoc Dunnett's multiple comparison test with T = 0 as reference (* $P < 0.05$). **E** Colony forming assay of HeLa cells non treated or treated with 2.5 or 5μM Pr-MPO in presence or absence of 5mM pyruvate. **F** HeLa cells treated without or with 5μM Pr-MPO alone or in presence of 5mM pyruvate at 0, 30, 60, 120 and 240 min were analyzed using western blotting to evaluate the degree of phosphorylation of PDH Ser93 residue

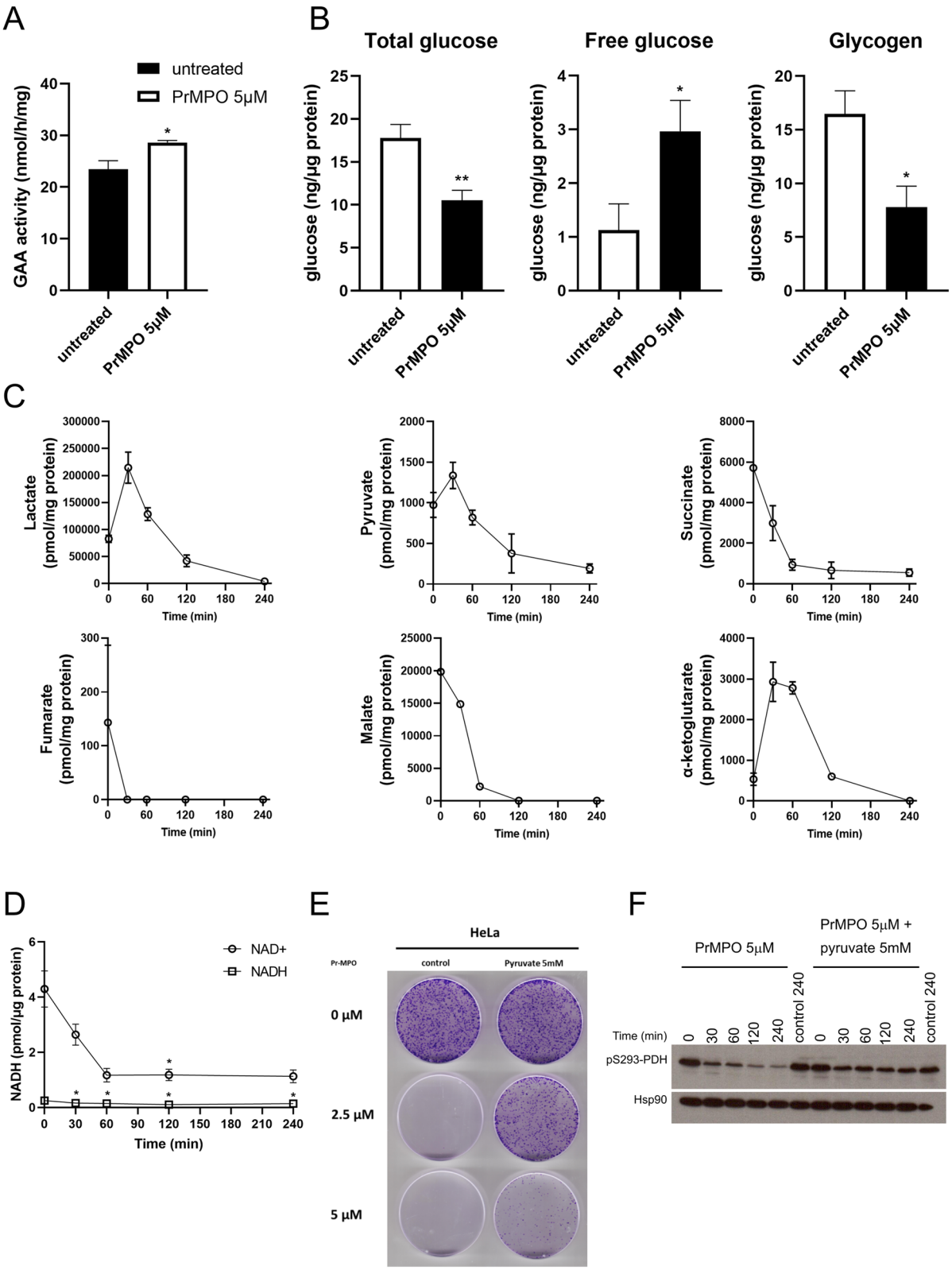

Fig. 6 (See legend on previous page.)

Consistent with the impairment of lysosomal machinery, an increase in the enzymatic activity of GAA, an important factor in the passive breakdown of glycogen in lysosomes, was observed. These results were corroborated by the levels of free glucose and glycogen degradation within two hours of treatment. The latter would be indicative of a compensatory response to maintain glucose levels, however, as the glycogen concentration fell below that of free glucose, the total amount of glucose within cells rapidly dropped to reach near depletion. That glucose metabolism appears to be a target of the lanthanide conjugate was further validated by the observation that TCA cycle associated organic acids, except citrate, as well as the glycolytic end products pyruvate and lactate were virtually completely depleted. This was accompanied by a robust decrease in NAD^+/NADH levels, thus indicating severe bioenergetic crisis. These results suggest a point of intervention upstream of TCA intermediates, probably at the level of glycolysis, thereby preventing pyruvate production. The critical role of pyruvate is supported by the rescue effect observed upon the addition of exogenous pyruvate. The cells' response to compensate for pyruvate loss appeared to be twofold: (1) upstream, through the mobilization of glucose stores which failed due to the inability of glycolysis to produce pyruvate and (2) downstream, by stimulating PDH activity as evidenced by the decrease in PDH S293 phosphorylation as a compensatory mechanism, which however failed since there was no pyruvate available as a substrate.

Interestingly, the biological activity of Pr-MPO was dependent upon the availability of serum and a non-protein component in the culture medium, which was identified and verified as Zn^{2+}. The protective effect of exogenous pyruvate also suggested a role for Zn^{2+} in Pr-MPO-dependent cell death [44–46]. To that end, Zn^{2+} has been shown to impair cellular energy production via inhibition of PK, glyceraldehyde-3-phosphate dehydrogenase and phosphofructokinase as well as mitochondrial aconitase, α-ketoglutarate dehydrogenase complex and cytochrome c oxidase [47–50]. The effect of TPEN, a Zn^{2+} chelator, to inhibit Pr-MPO induced cellular and biochemical effects, and conversely the ability of exogenously added Zn^{2+} to restore Pr-MPO-induced cell death strongly corroborate the involvement of Zn^{2+}. Consistent with that, the anti-viral activity of the pyrithione group alone (MPO) has been attributed to its ability to act as a Zn^{2+} ionophore [51, 52]. Indeed, the fact that the presence of Zn^{2+} significantly lowered the effective concentration of Pr-MPO and the active uptake of Zn^{2+}, induced upon exposure to the lanthanide compound, suggest Zn^{2+} toxicity as the mechanism of anti-tumor activity.

Metal ionophores have been proposed as a new class of anticancer agents displaying selectivity toward cancer cells with minimal off target side effects [53]. To that end, Zn^{2+} ionophores, clioquinol and PCI-5002, have been shown to disrupt lysosomal integrity and promote autophagic cell death, respectively [54, 55]. In another study, Zn^{2+} oxide nanoparticles were shown to induce autophagosome formation but preventing their maturation [56]. Notably, among Zn^{2+} ionophores the most interesting is Zn-pyrithione, an FDA approved compound. Zn-pyrithione is a 2:1 coordination complex between Zn^{2+} and two molecules of pyrithione, which is similar in structure to Pr-MPO with 3:1 coordination complex between Pr and three MPO groups. Zn-pyrithione has been shown to trigger apoptosis in ovarian and cervical cancer cells, necrosis in prostate cancer cancers,

(See figure on next page.)

Fig. 7 Pr-MPO induces cell death through Zn^{2+}-mediated toxicity. **A** Effect of 5μM Pr-MPO treatment on HeLa cells using a 0% FBS culture medium supplemented with 1 or 2μM sodium acetate (NaAc) or zinc acetate (ZnAc). Statistical analysis was performed using One-way ANOVA followed by a post-hoc Dunnett's multiple comparison test using the condition Pr-MPO 5μM as a control reference (** $P < 0.01$, *** $P < 0.005$). **B** Rescue effect of the Zn^{2+} chelator TPEN (0.5 and 2.5μM) on HeLa cells treated with 5μM Pr-MPO. Statistical analysis was performed using One-way ANOVA followed by a post-hoc Dunnett's multiple comparison test using the untreated cell condition as a control reference (**** $P < 0.0001$). **C** Colony forming assay of untreated HeLa cells or treated with 5μM Pr-MPO, 500μM ZnAc, 2.5μM TPEN, 2.5μM TPEN + 5μM Pr-MPO or 2.5μM TPEN + 5μM Pr-MPO + 5μM ZnAc. **D** Western blot analysis of HeLa cells treated for 2 h with DMF, 5μM Pr-MPO and 500μM ZnAc; or DMF, 5μM Pr-MPO and 5μM Pr-MPO + 5μM in presence of 5μM TPEN; or DMF and 5μM Pr-MPO in presence of 0.1μM Bafilomycin A1; or DMF and 5μM Pr-MPO in presence of 500μM EDHB (iron chelator); or 200μM DCA (positive control) and 25μM LY30 (negative control). The level of Ser293 phosphorylation of PDH and total PDH was assessed as well as the autophagy marker LC3. This figure shows the results of the same samples run through two different gels: one gel was used to probe actin and S293PDH while the second gel was used to probe actin, total PDH and LC3; the use of two gels was necessary due to the strong resilience of the S293PDH antibody to stripping buffer. **E** Measure of total glucose, free glucose, glycogen and lactate in untreated HeLa cells or treated with 5μM Pr-MPO, 500μM ZnAc, 2.5μM TPEN, 2.5μM TPEN + 5μM Pr-MPO or 2.5μM TPEN + 5μM Pr-MPO + 5μM ZnAc. Statistical analysis was performed using One-way ANOVA followed by a post-hoc Dunnett's multiple comparison test using the untreated cell condition as a control reference (* $P < 0.05$, ** $P < 0.01$, *** $P < 0.005$, **** $P < 0.0001$). **F** Measure of intracellular pH in untreated HeLa cells or treated with 5μM Pr-MPO, 500μM ZnAc, 2.5μM TPEN, 2.5μM TPEN + 5μM Pr-MPO or 2.5μM TPEN + 5μM Pr-MPO + 5μM ZnAc. Statistical analysis was performed using One-way ANOVA followed by a post-hoc Dunnett's multiple comparison test using the untreated cell condition as a control reference (* $P < 0.05$, ** $P < 0.01$, *** $P < 0.005$)

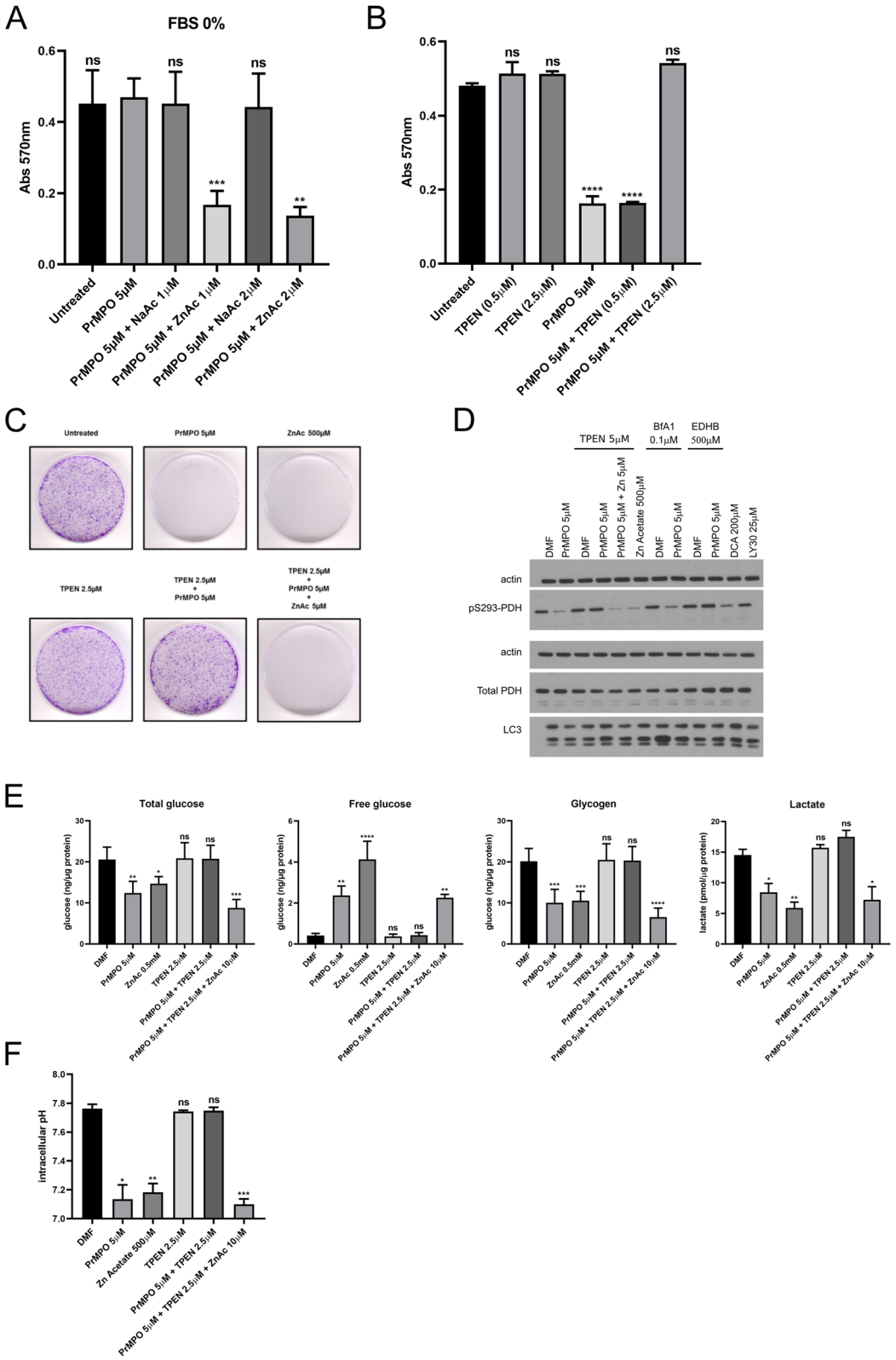

Fig. 7 (See legend on previous page.)

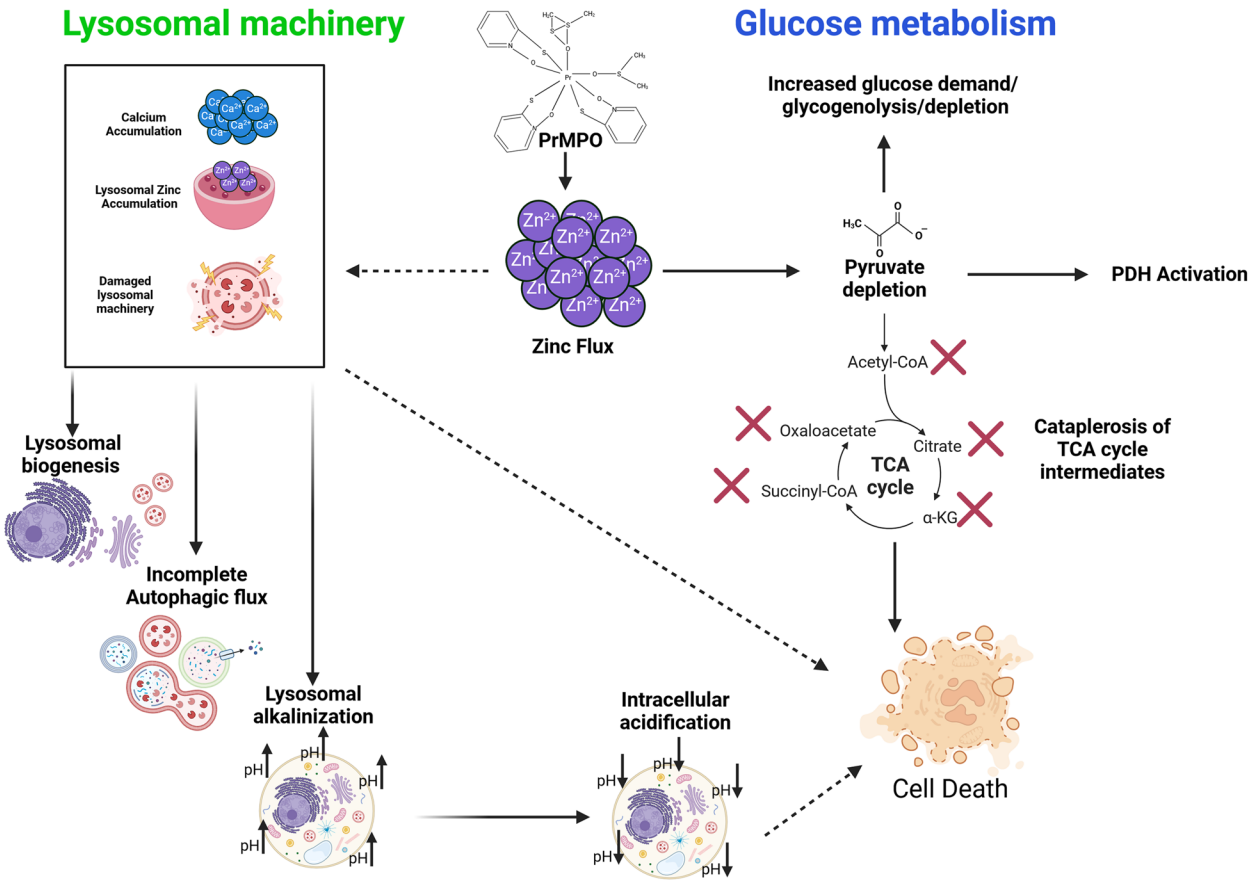

Fig. 8 Schematic diagram on the anti-cancer effects of Pr-MPO. Exposure of cells to Pr-MPO results in early lysosomal accumulation of Ca^{2+} that triggers lysosomal biogenesis, cytosolic acidification, and incomplete autophagy. The death inducing effects are mediated by Zn^{2+} import that results in pyruvate depletion and cataplerosis of TCA intermediates. Image created in BioRender. Pervaiz, S. (2023) BioRender.com/b20z095

and inhibition of proteasome-associated deubiquitinase in leukemia and lung cancer cells [57–60]. Furthermore, Zn-pyrithione emerged as a promising compound from a screen of chemical libraries exhibiting potent growth inhibitory, apoptosis inducing, mTOR inhibitory, and pyruvate kinase inhibitory activities [61]. This effect was confirmed in vivo in a xenograft model in which tumor growth was strongly inhibited with minimal toxicity to the normal tissues such as kidneys and liver, which is much similar to the in vivo data presented in the present study with Pr-MPO. Taken together, these published reports provide strong support to our findings highlighting the therapeutic potential of a lanthanide-MPO conjugate that functions as a Zn^{2+} ionophore.

Conclusions and translational relevance

The data presented in this communication highlights the therapeutic potential of Pr-MPO, a lanthanide conjugate, by providing a comprehensive insight into the molecular mechanism triggered in cancer cells, irrespective of their phenotype. These alterations include metabolic processes that endow cancer cells with a survival advantage, in particular glycolysis and lysosomal machinery (schematic Fig. 8). The consensus, based on published reports, is that lanthanide-based compounds are relatively safe to administer with no major side effects. For example, galodinium-based nanoparticles have been shown to radio-sensitize cancer cells while having minimum toxicity due to efficient clearance by the kidneys. Our data also links Zn^{2+} uptake and its ability to deregulate lysosomal function, promote intracellular acidification and induce cataplerosis, thereby shutting down critical survival associated cellular processes (Fig. 8). This is a point of interest as it targets two mechanisms known to be crucial for cancer cell survival. Pyruvate can rescue cancer cells as it provides the key metabolite targeted by Pr-MPO, thereby salvaging mitochondrial metabolism despite Zn^{2+} toxicity. While exogenous pyruvate counters only the effect related to glucose metabolism, upstream inhibition of Zn^{2+} toxicity by TPEN blocks the lysosomal effects of Pr-MPO. Importantly, FDA-approved Zn^{2+} ionophores

are already available and could be repurposed. However, some questions remain to be addressed to fully understand Zn^{2+}-induced toxicity triggered by Zn^{2+} ionophore such as Pr-MPO, particularly its relationship to Ca^{2+} mobilization during the treatment. Studies on Zn^{2+} toxicity have highlighted the existence of a cross-talk with Ca^{2+}-related mechanisms and both Zn^{2+} and Ca^{2+} appear to be tightly interconnected. Despite the fact that Ca^{2+}-controlled mechanisms or Zn^{2+} overloading has been mostly associated with neurotoxicity [62–64], such a connection between Zn^{2+} and Ca^{2+} ions could provide novel insight into stress signaling involving lysosomal impairment and metabolic catastrophe. Another simpler explanation could be the possibility of Zn^{2+} reacting with the fluorescent probe(s) used for measuring intracellular Ca^{2+} as previously reported in studies involving Zn^{2+} neurotoxicity [65, 66].

Supplementary Information

The online version contains supplementary material available at https://doi.org/10.1186/s12964-024-01883-5.

Supplementary Material 1.

Supplementary Material 2.

Acknowledgements
Some of the data presented in the manuscript are adapted from the doctoral thesis (2015) of Dan Liu, NUS Graduate School and Department of Physiology, YLL School of Medicine, National University of Singapore, Singapore. The authors would like to thank Ms. Amanda Ng and Mr. Geoffrey Balamurli for their contributions to the project. This work was supported by grants from the National Medical Research Council (NMRC/1214/2009) and Ministry of Education (MOE/2013-T2-2-130), Singapore, to S.P.

Declaration of Conflict
None of the authors have any conflict to declare.

Authors' contributions
G.L.B: Generated data and figures and analyzed data and wrote the first draft. D.L: Generated data and figures and analyzed data. M.F: Assisted with the intracellular Ca^{2+} measurements and live imaging. S.K.Y: Synthesized the lanthanide conjugate and conducted the in vivo work. C.K: Assisted in electron microscopy and its analysis. S.P: Conceptualized, funded and supervised the work, analyzed the data and wrote the manuscript.

Data availability
Data presented in the manuscript can be made available upon request to the corresponding author.

Declarations

Competing interests
The authors declare no competing interests.

Author details
[1]Department of Physiology, Yong Loo Lin School of Medicine, National University of Singapore (NUS), Singapore 117597, Singapore. [2]Integrative Science and Engineering Programme (ISEP), NUS Graduate School (NUSGS), NUS, Singapore, Singapore. [3]Program in Neuroscience and Behavioral Disorders. Duke-NUS Medical School, Singapore, Singapore. [4]Department of Anatomy, Yong Loo Lin School of Medicine, NUS, Singapore, Singapore. [5]NUS Centre for Cancer Research (N2CR), Yong Loo Lin School of Medicine, NUS, Singapore, Singapore. [6]National University Cancer Institute, National University Health System, Singapore, Singapore. [7]Present address: reMYND NV. Bio-Incubator, Leuven, Belgium.

Received: 15 August 2024 Accepted: 7 October 2024
Published online: 19 October 2024

References

1. Akman M, Belisario DC, Salaroglio IC, et al. Hypoxia, endoplasmic reticulum stress and chemoresistance: dangerous liaisons. J Exp Clin Cancer Res. 2021;40(1):28.
2. Assaraf YG, Brozovic A, Gonçalves AC, et al. The multi-factorial nature of clinical multidrug resistance in cancer. Drug Resist Updat. 2019;46:100645.
3. Bach DH, Hong JY, Park HJ, Lee SK. The role of exosomes and miRNAs in drug-resistance of cancer cells. Int J Cancer. 2017;141(2):220–30.
4. Chong SJF, Iskandar K, Lai JXH, et al. Serine-70 phosphorylated Bcl-2 prevents oxidative stress-induced DNA damage by modulating the mitochondrial redox metabolism. Nucleic Acids Res. 2020;48(22):12727–45.
5. Chong SJF, Zhu F, Dashevsky O et al. Hyperphosphorylation of BCL-2 family proteins underlies functional resistance to venetoclax in lymphoid malignancies. J Clin Invest. 2023;133(22).
6. Hirpara J, Eu JQ, Tan JKM, et al. Metabolic reprogramming of oncogene-addicted cancer cells to OXPHOS as a mechanism of drug resistance. Redox Biol. 2019;25:101076.
7. Kelland L. The resurgence of platinum-based cancer chemotherapy. Nat Rev Cancer. 2007;7(8):573–84.
8. Rottenberg S, Disler C, Perego P. The rediscovery of platinum-based cancer therapy. Nat Rev Cancer. 2021;21(1):37–50.
9. Mohapatra P, Shriwas O, Mohanty S et al. CMTM6 drives cisplatin resistance by regulating wnt signaling through the ENO-1/AKT/GSK3β axis. JCI Insight. 2021;6(4).
10. Xiao Y, Lin FT, Lin WC. ACTL6A promotes repair of cisplatin-induced DNA damage, a new mechanism of platinum resistance in cancer. Proc Natl Acad Sci U S A. 2021;118(3).
11. Lazarević T, Rilak A, Bugarčić ŽD. Platinum, palladium, gold and ruthenium complexes as anticancer agents: current clinical uses, cytotoxicity studies and future perspectives. Eur J Med Chem. 2017;142:8–31.
12. Teo RD, Termini J, Gray HB. Lanthanides: applications in Cancer diagnosis and therapy. J Med Chem. 2016;59(13):6012–24.
13. Pałasz A, Czekaj P. Toxicological and cytophysiological aspects of lanthanides action. Acta Biochim Pol. 2000;47(4):1107–14.
14. Bottrill M, Kwok L, Long NJ. Lanthanides in magnetic resonance imaging [10.1039/B516376P]. Chem Soc Rev. 2006;35(6):557–71.
15. Naccache R, Rodríguez EM, Bogdan N, et al. High resolution fluorescence imaging of cancers using lanthanide ion-doped upconverting nanocrystals. Cancers (Basel). 2012;4(4):1067–105.
16. Shi XM, Tang RR, Gu GL, Huang KL. Synthesis and fluorescence properties of lanthanide(III) complexes of a novel bis(pyrazolyl-carboxyl) pyridine-based ligand. Spectrochim Acta Mol Biomol Spectrosc. 2009;72(1):198–203.
17. Fricker SP. The therapeutic application of lanthanides [10.1039/B509608C]. Chem Soc Rev. 2006;35(6):524–33.
18. Wang K, Li R, Cheng Y, Zhu B. Lanthanides—the future drugs? Coordination Chemistry Reviews. 1999;190–192:297–308.
19. Zhang J, Li Y, Hao X, et al. Recent progress in therapeutic and diagnostic applications of lanthanides. Mini Rev Med Chem. 2011;11(8):678–94.
20. Gerken LRH, Keevend K, Zhang Y, et al. Lanthanide-Doped Hafnia nanoparticles for Multimodal Theranostics: tailoring the Physicochemical Properties and interactions with Biological entities. ACS Appl Mater Interfaces. 2019;11(1):437–48.
21. Alptürk O, Rusin O, Fakayode SO, et al. Lanthanide complexes as fluorescent indicators for neutral sugars and cancer biomarkers. Proc Natl Acad Sci U S A. 2006;103(26):9756–60.
22. Lux F, Tran VL, Thomas E, et al. AGuIX(®) from bench to bedside-transfer of an ultrasmall theranostic gadolinium-based nanoparticle to clinical medicine. Br J Radiol. 2019;92(1093):20180365.

23. Liu Y, Chen C, Qian P, et al. Gd-metallofullerenol nanomaterial as non-toxic breast cancer stem cell-specific inhibitor. Nat Commun. 2015;6:5988.
24. Reed KC, Bygrave FL. The inhibition of mitochondrial calcium transport by lanthanides and ruthenium red. Biochem J. 1974;140(2):143–55.
25. Brayshaw LL, Smith RCG, Badaoui M, et al. Lanthanides compete with calcium for binding to cadherins and inhibit cadherin-mediated cell adhesion [10.1039/C8MT00317C]. Metallomics. 2019;11(5):914–24.
26. Palizban AA, Sadeghi-Aliabadi H, Abdollahpour F. Effect of cerium lanthanide on Hela and MCF-7 cancer cell growth in the presence of transferring. Res Pharm Sci. 2010;5(2):119–25.
27. Kaczmarek MT, Zabiszak M, Nowak M, Jastrzab R. Lanthanides Schiff base complexes, applications in cancer diagnosis, therapy, and antibacterial activity. Coord Chem Rev. 2018;370:42–54.
28. Benedetto A, Bocca C, Brizio P, et al. Effects of the rare elements lanthanum and cerium on the growth of colorectal and hepatic cancer cell lines. Toxicol Vitro. 2018;46:9–18.
29. Abdukayum A, Chen JT, Zhao Q, Yan XP. Functional near infrared-emitting Cr3+/Pr3 + co-doped zinc gallogermanate persistent luminescent nanoparticles with superlong afterglow for in vivo targeted bioimaging. J Am Chem Soc. 2013;135(38):14125–33.
30. Mandl GA, Van der Heggen D, Cooper DR, et al. On a local (de-) trapping model for highly doped Pr3 + radioluminescent and persistent luminescent nanoparticles [10.1039/D0NR06577C]. Nanoscale. 2020;12(40):20759–66.
31. Shrestha S, Yeung CM, Mills CE, et al. Chemically immobilized single-stranded oligonucleotides on praseodymium oxide nanoparticles as an unlabeled DNA sensor probe using impedance. Angew Chem Int Ed Engl. 2007;46(21):3855–9.
32. Müller M, Espinoza S, Jüstel T, et al. UVC-Emitting LuPO(4):pr(3+) nanoparticles decrease Radiation Resistance of Hypoxic Cancer cells. Radiat Res. 2020;193(1):82–7.
33. Ferreira MC, Podder TK, Rasmussen KH, Jung JW. Praseodymium-142 microspheres for brachytherapy of nonresectable hepatic tumors. Brachytherapy. 2013;12(6):654–64.
34. Koyuncu N, Reyhancan İA. Dose evaluation of 142Pr radioisotope by Monte Carlo method in eye brachytherapy. Radiat Phys Chem. 2020;177:109150.
35. Yeltepe E, Yücel H. Standardization of 142Pr activity concentration. Appl Radiat Isot. 2018;134:263–8.
36. Hirpara JL, Loh T, Ng SB, et al. Aberrant localization of apoptosis protease activating factor-1 in lipid raft sub-domains of diffuse large B cell lymphomas. Oncotarget. 2016;7(51):83964–75.
37. Holme AL, Yadav SK, Pervaiz S. Automated laser scanning cytometry: a powerful tool for multi-parameter analysis of drug-induced apoptosis. Cytometry A. 2007;71(2):80–6.
38. Lee SF, Hirpara JL, Qu J, et al. Identification of a novel catalytic inhibitor of topoisomerase II alpha that engages distinct mechanisms in p53(wt) or p53(-/-) cells to trigger G2/M arrest and senescence. Cancer Lett. 2022;526:284–303.
39. Li RJ, Xu J, Fu C et al. Regulation of mTORC1 by lysosomal calcium and calmodulin. Elife. 2016;5.
40. Porter K, Nallathambi J, Lin Y, Liton PB. Lysosomal basification and decreased autophagic flux in oxidatively stressed trabecular meshwork cells: implications for glaucoma pathogenesis. Autophagy. 2013;9(4):581–94.
41. Persi E, Duran-Frigola M, Damaghi M, et al. Systems analysis of intracellular pH vulnerabilities for cancer therapy. Nat Commun. 2018;9(1):2997.
42. Rebecca VW, Nicastri MC, McLaughlin N, et al. A Unified Approach to Targeting the Lysosome's degradative and Growth Signaling roles. Cancer Discov. 2017;7(11):1266–83.
43. Li Z, Zhu YT, Xiang M, et al. Enhanced lysosomal function is critical for paclitaxel resistance in cancer cells: reversed by artesunate. Acta Pharmacol Sin. 2021;42(4):624–32.
44. Chang I, Cho N, Koh JY, Lee MS. Pyruvate inhibits zinc-mediated pancreatic islet cell death and diabetes. Diabetologia. 2003;46(9):1220–7.
45. Lee JY, Kim YH, Koh JY. Protection by pyruvate against transient forebrain ischemia in rats. J Neurosci. 2001;21(20):Rc171.
46. Yoo MH, Lee JY, Lee SE, et al. Protection by pyruvate of rat retinal cells against zinc toxicity in vitro, and pressure-induced ischemia in vivo. Invest Ophthalmol Vis Sci. 2004;45(5):1523–30.
47. Dineley KE, Votyakova TV, Reynolds IJ. Zinc inhibition of cellular energy production: implications for mitochondria and neurodegeneration. J Neurochem. 2003;85(3):563–70.
48. Matheson BK, Adams JL, Zou J, et al. Effect of metabolic inhibitors on ATP and citrate content in PC3 prostate cancer cells. Prostate. 2007;67(11):1211–8.
49. Murakami K, Yoshino M. Zinc inhibition of pyruvate kinase of M-type isozyme. Biometals. 2017;30(3):335–40.
50. Sheline CT, Behrens MM, Choi DW. Zinc-induced cortical neuronal death: contribution of energy failure attributable to loss of NAD(+) and inhibition of glycolysis. J Neurosci. 2000;20(9):3139–46.
51. Krenn BM, Gaudernak E, Holzer B, et al. Antiviral activity of the zinc ionophores pyrithione and hinokitiol against picornavirus infections. J Virol. 2009;83(1):58–64.
52. Qiu M, Chen Y, Chu Y, et al. Zinc ionophores pyrithione inhibits herpes simplex virus replication through interfering with proteasome function and NF-κB activation. Antiviral Res. 2013;100(1):44–53.
53. Ding WQ, Lind SE. Metal ionophores - an emerging class of anticancer drugs. IUBMB Life. 2009;61(11):1013–8.
54. Kim KW, Speirs CK, Jung DK, Lu B. The zinc ionophore PCI-5002 radiosensitizes non-small cell lung cancer cells by enhancing autophagic cell death. J Thorac Oncol. 2011;6(9):1542–52.
55. Yu H, Zhou Y, Lind SE, Ding WQ. Clioquinol targets zinc to lysosomes in human cancer cells. Biochem J. 2009;417(1):133–9.
56. Liu Z, Lv X, Xu L, et al. Zinc oxide nanoparticles effectively regulate autophagic cell death by activating autophagosome formation and interfering with their maturation. Part Fibre Toxicol. 2020;17(1):46.
57. Carraway RE, Dobner PR. Zinc pyrithione induces ERK- and PKC-dependent necrosis distinct from TPEN-induced apoptosis in prostate cancer cells. Biochim Biophys Acta. 2012;1823(2):544–57.
58. Chen M, Ding Y, Ke Y, et al. Anti-tumour activity of zinc ionophore pyrithione in human ovarian cancer cells through inhibition of proliferation and migration and promotion of lysosome-mitochondrial apoptosis. Artif Cells Nanomed Biotechnol. 2020;48(1):824–33.
59. Rudolf E, Cervinka M. Zinc pyrithione induces cellular stress signaling and apoptosis in Hep-2 cervical tumor cells: the role of mitochondria and lysosomes. Biometals. 2010;23(2):339–54.
60. Zhao C, Chen X, Yang C, et al. Repurposing an antidandruff agent to treating cancer: zinc pyrithione inhibits tumor growth via targeting proteasome-associated deubiquitinases. Oncotarget. 2017;8(8):13942–56.
61. Srivastava G, Matta A, Fu G, et al. Anticancer activity of pyrithione zinc in oral cancer cells identified in small molecule screens and xenograft model: implications for oral cancer therapy. Mol Oncol. 2015;9(8):1720–35.
62. Granzotto A, Canzoniero LMT, Sensi SL. A neurotoxic Menage-a-trois: glutamate, calcium, and Zinc in the Excitotoxic Cascade. Front Mol Neurosci. 2020;13:600089.
63. Hershfinkel M. Cross-talk between zinc and calcium regulates ion transport: a role for the zinc receptor, ZnR/GPR39. J Physiol. 2024;602(8):1579–94. https://doi.org/10.1113/JP283834.
64. Kim YH, Eom JW, Koh JY. Mechanism of Zinc Excitotoxicity: a focus on AMPK. Front Neurosci. 2020;14:577958.
65. Inoue K, Branigan D, Xiong ZG. Zinc-induced neurotoxicity mediated by transient receptor potential melastatin 7 channels. J Biol Chem. 2010;285(10):7430–9.
66. Stork CJ, Li YV. Intracellular zinc elevation measured with a calcium-specific indicator during ischemia and reperfusion in rat hippocampus: a question on calcium overload. J Neurosci. 2006;26(41):10430–7.

Publisher's note